Pure Appl. Geophys. 173 (2016), 4139–4178

DOI 10.1007/s00024-016-1407-8

Pure and Applied Geophysics

A Comparative Analysis of Coastal and Open-Ocean Records of the Great Chilean Tsunamis of 2010, 2014 and 2015 off the Coast of Mexico

OLEG ZAYTSEV,[1] ALEXANDER B. RABINOVICH,[2,3] and RICHARD E. THOMSON[2]

Abstract—The three great earthquakes off the coast of Chile on 27 February 2010 (Maule, M_w 8.8), 1 April 2014 (Iquique, M_w 8.2) and 16 September 2015 (Illapel, M_w 8.3) generated major transoceanic tsunamis that spread throughout the Pacific Ocean and were measured by numerous coastal tide gauges and open-ocean DART stations. Statistical and spectral analyses of the tsunami waves from the events recorded on the Pacific coast of Mexico enabled us to estimate parameters of the waves along the coast and to compare statistical features of the events. We also identified three coastal "hot spots" (sites having maximum tsunami risk): Puerto Angel, Puerto Madero and Manzanillo. Based on the joint spectral analyses of the tsunamis and background noise, we have developed a method for using coastal observations to determine the underlying spectrum of tsunami waves in the deep ocean. The "reconstructed" open-ocean tsunami spectra are in close agreement with the actual tsunami spectra evaluated from direct analysis of the DART records offshore of Mexico. We have further used the spectral estimates to parameterize the energy of the three Chilean tsunamis based on the total open-ocean tsunami energy and frequency content of the individual events.

Key words: Chilean earthquakes and tsunamis, Mexican coast, tide gauge records, DART, open-ocean tsunamis, tsunami travel time, spectral analysis.

1. Introduction

The subduction zone located along the Peru–Chile Trench, where the Nazca Plate subducts beneath the South American Plate, is one of the most active seismic zones on Earth. Great earthquakes (with $M_w > 8.0$) occur in this zone on a regular basis (Kulikov et al. 2005; Fujii and Satake 2013) and generate destructive tsunamis that propagate throughout the Pacific Ocean, causing widespread damage and loss of life in distant regions. The tsunami from the Great Chile Earthquake of 22 May 1960 (M_w 9.5), the strongest event instrumentally recorded in the World Ocean, was responsible for the deaths of 61 people in the Hawaiian Islands, 142 in Japan and 32 in the Philippines. Tsunami wave heights of several meters were observed along the coasts of California, mainland Alaska, the Aleutian Islands, Japan and Russia at distances of 13,000–18,000 km from the source area. This particular tsunami stimulated strong international cooperation in the tsunami research and resulted in the establishment of the International Tsunami Warning System in the Pacific Ocean (ITSU) (Igarashi et al. 2011). Tsunamis originating offshore of Chile and Peru are considered as the major threat for the coasts of Pacific islands, New Zealand, Hawaii, California, Japan and Russia. Joint international efforts are key factors to help mitigate the tsunami hazard from the Chilean earthquakes and to provide an effective tsunami warning for the Pacific Ocean.

Three great earthquakes occurred offshore of Chile during the period 2010–2015 (Fig. 1). The 27 February 2010 Maule earthquake (M_w 8.8) was the strongest in this region since 1960 and one of the most intense earthquakes ever recorded. The 1 April 2014 Iquique (M_w 8.2) and the 16 September 2015 Illapel (M_w 8.3) earthquakes were also devastating events. The potential energy of the powerful 2010 earthquake was 7.26×10^{14} J, while the energies of the 2014 and 2015 earthquakes are estimated as 1.99×10^{13} J and 8.15×10^{13} J, respectively (Omira et al. 2016). The

---

[1] Instituto Politécnico Nacional, Centro Interdisciplinario de Ciencias Marinas, Ave. IPN, s/n, Playa Palo de Santa Rita, 23096 La Paz, BCS, Mexico.

[2] Department of Fisheries and Oceans, Institute of Ocean Sciences, 9860 West Saanich Road, Sidney, BC V8L 4B2, Canada. E-mail: A.B.Rabinovich@gmail.com

[3] Russian Academy of Sciences, P.P. Shirshov Institute of Oceanology, 36 Nakhimovsky Prosp., Moscow 117997, Russia.

Birkhäuser

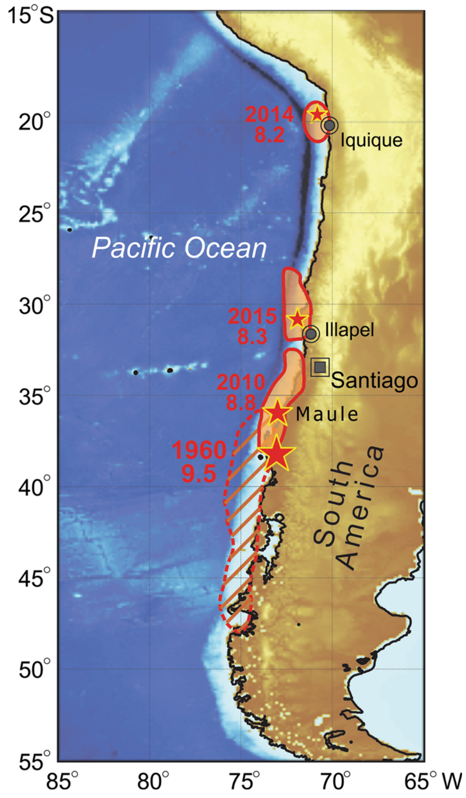

Figure 1

Map of the Pacific coast of South America showing the tsunami source region for the 1960 Great Chile Earthquake (M_w 9.5) (hatched area with *red dashed border*), and source areas for the 2010 (M_w 8.8), 2014 (M_w 8.2) and 2015 (M_w 8.3) Chilean earthquakes (*pink areas* with *solid red border lines*). The earthquake epicenters are indicated by *red stars*

earthquakes generated major transoceanic tsunamis that spread over the Pacific Ocean (Fig. 2) and were recorded by numerous open-ocean bottom pressure stations and coastal tide gauges (cf. Borrero and Greer 2013; Shevchenko et al. 2013; Rabinovich et al. 2013a, b; Heidarzadeh et al. 2015, 2016; Eblé et al. 2015; Tang et al. 2016; Omira et al. 2016). Intense currents associated with these events were observed in New Zealand, California and Japan; currents induced by the 2010 tsunami caused severe damage in ports and harbours of southern California (Wilson et al. 2010, 2013).

All three Chilean tsunamis were recorded on the Pacific coast of Mexico. Although there was no documented damage associated with these events, currents induced in certain bays and harbours were

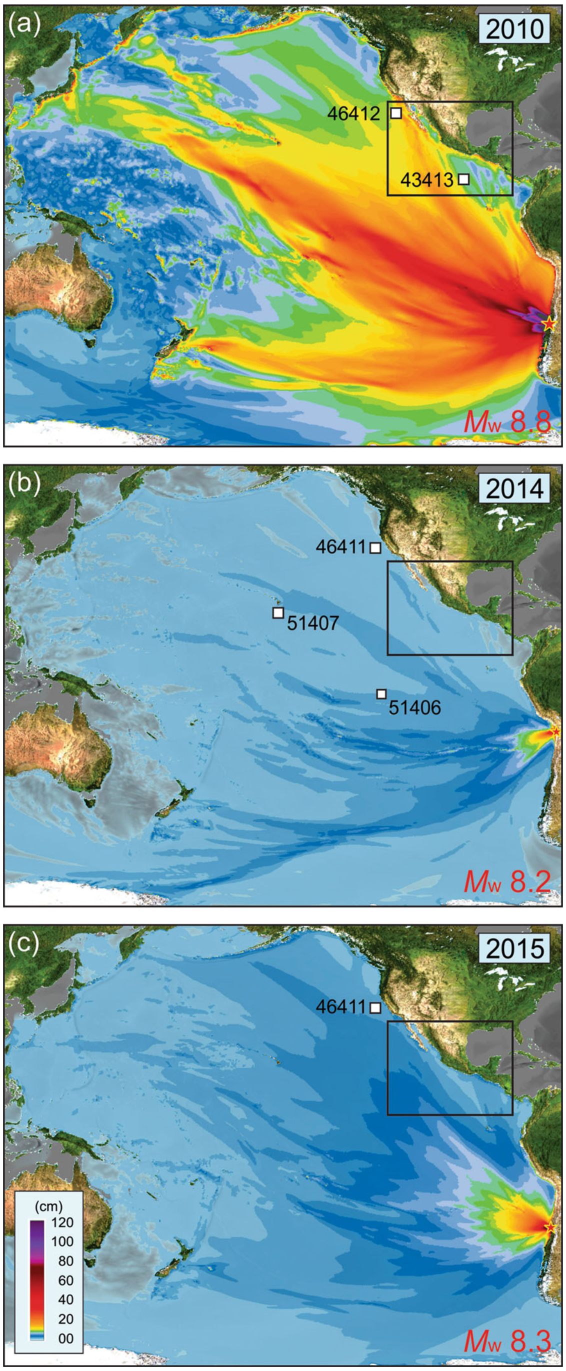

Figure 2

NOAA/PMEL numerically simulated maximum tsunami amplitudes for the **a** 2010, **b** 2014, and **c** 2015 Chilean tsunamis in the Pacific Ocean (courtesy of Vasily Titov and Rachel Tang). The earthquake epicenters are indicated by *red stars*. The DART stations that have provided 15-s tsunami records for the different events are denoted by *white squares* strong and dangerous, similar to the case of California. In general, local and remote tsunamis present a considerable threat to the coast of Mexico (cf. Farreras and Sanchez 1991; Farreras et al. 2007). Significant tsunamis have been observed many times in this region in the past and are likely to occur in the near future. Sanchez and Farreras (1993) listed 21 tsunamis instrumentally recorded on the coast of Mexico for the period of 1952–1985; 12 of them were from distant source regions and nine from local source regions. The highest tsunami waves, with trough-to-crest heights of up to 2.5 m, were associated with the 1957 (Aleutian), 1960 (Chile) and 1964 (Alaska) earthquakes. However, all these observations were based on pen-and-paper analogue records, which limit the accuracy of the statistical and spectral estimates of the derived tsunami parameters. Sanchez and Farreras (1983) digitized 45 tide gauge records from 11 tsunamis measured at 12 coastal Mexican stations. They attempted to define some spectral features that could be related to specific events but, in general, their results were somewhat contradictive, probably because of the inadequate quality of the data.

A major upgrade of the existing Mexican tide gauge network was completed in the middle of the 1990s. The new digital instruments were designed to continuously measure sea level variations with much higher precision and time resolution than the earlier analogue gauges. During the last 20 years, a number of tsunamis have been digitally recorded on the coast of Mexico. However, to date, only a few of these records have been examined. Ortiz et al. (1998, 2000) used several tide records of the Jalisco-Colima tsunami generated by the local M_w 8.0 earthquake of 9 October 1995 to evaluate earthquake source parameters. Rabinovich et al. (2006, 2011) used three records of the 26 December 2004 Sumatra tsunami to estimate statistical parameters and energy decay for waves arriving on the coast of Mexico.

High-quality tide gauge measurements of the Chilean tsunamis of 2010, 2014 and 2015 have enabled us to estimate the main physical attributes of the tsunami waves, to examine changes in wave properties along the coast of Mexico, to compare particular features of the three events and to characterize these features against those of tsunamis at other locations in the Pacific Ocean. Most importantly, we have been able to compare the coastal records of the tsunamis with records from open-ocean DART[1] stations situated in deep-water off the Mexican coast. This allows us to investigate the spatial transformation of the incoming tsunami waves and to estimate general energy related characteristics of the three events in the open ocean. Comparison of the characteristics and frequency composition of the three tsunamis is of broad scientific interest and important for the evaluation of tsunami risk for the Pacific coastal areas of Mexico.

2. *Observations*

The 2010, 2014 and 2015 Chilean tsunamis were measured on the Pacific coast and offshore of Mexico by a number of high-quality digital coastal tide gauges and by NOAA DART bottom pressure recorders, (BPRs; Fig. 3). The tide gauge network on the Pacific coast of Mexico consists of two major components:

1. The National Mareographic Service, operated by the Institute of Geophysics, National Autonomous University of Mexico (UNAM), which includes 10 digital tide gauges along the Pacific coast of Mexico (http://www.mareografico.unam.mx; see white circles in Fig. 3). All tide gauges have a radar sensor and satellite data transmission system. Some have an additional float sensor. Sea level changes in 2010 were recorded every 6 min while those in 2014 and 2015 were recorded every 1 min.
2. The Northwestern net of sea level monitoring, operated by the Laboratory of Sea Level, Center for Scientific Research and Higher Education (CICESE), Ensenada, and consisting of 11 tide gauges, of which five could be used for the present study (yellow circles in Fig. 3 plus Acapulco with both UNAM and CICESE instruments). Several tide gauges combine the main radar sensor with a

---

[1] DART = Deep-ocean Assessment and Reporting of Tsunamis, is an effective network of deep-ocean stations elaborated for continuous monitoring of tsunami waves in the open ocean and early tsunami warning (cf. Titov 2009; Mofjeld 2009; Mungov et al. 2013; Rabinovich and Eblé 2015).

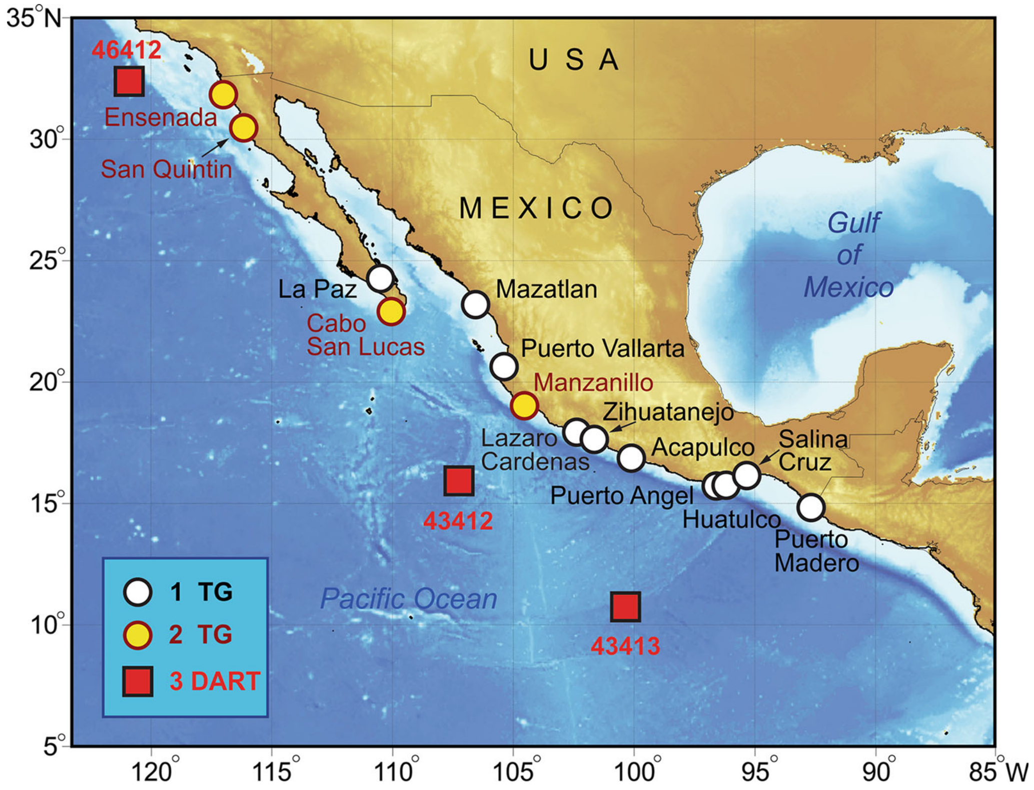

Figure 3
Map of coastal Mexico showing the location of tide gauges operated by UNAM (*1*), CICESE (*2*), and the three open-ocean DART stations (*3*) located near the coast of Mexico

bottom pressure sensor. Sea level data are stored at 1 min intervals and, for certain periods of time, at 1-s or 6-s time resolution (http://www.redmar.cicese.mx).

The primary purpose of the Mexican tide gauge network is to measure relatively low-frequency processes, such as tides, storm surges, and seasonal sea level variations (Farreras and Sanchez 1991). As a consequence, some tide gauges have been installed at locations that are not optimal for tsunami monitoring, namely in sheltered ports or harbours having narrow and shallow entrances. The stations having this limitation are: San Quintin, Lazaro Cardenas, Puerto Madero, Salina Cruz and, to a more limited extent, Manzanillo and Cabo San Lucas.

Some of the tide gauges were not in operation during the 2010, 2014 and 2015 Chilean tsunamis or had serious technical problems, rendering them unusable for our study. However, all properly working instruments clearly indicated the presence of tsunami waves. Most of the tide gauge data used in our analyses were obtained from the UNAM and CICESE, but a few records were also obtained from the National Tsunami Warning Center (NTWC), Palmer, Alaska. Table 1 summarizes the coastal data available for each event. For three stations (Acapulco, Manzanillo and Puerto Madero), the data are from two different sources.

We have also used two types of offshore DART data in our examination of the three Chilean events (see Mungov et al. 2013 and Rabinovich and Eblé 2015 for a description of the DART data):

1. “Event mode” data, which are transmitted after the start of the event in real-time for several hours at pre-defined 1-min intervals.
2. 15-s tsunami data, which are stored in the instrument package and then downloaded following the DART BPR retrieval.

Table 1

Tide gauges and DART stations that recorded the 2010, 2014 and 2015 Chilean tsunamis on the Pacific coast and offshore of Mexico

No.	Station (DART ocean depth)	Data source	Coordinates		Sampling interval (min)		
			Latitude °N	Longitude °W	Tsunami event		
					2010	2014	2015
1	Ensenada	CICESE	31° 50.9′	116° 37.1′	–	1	1
2	San Quintin	CICESE	30° 33.0′	115° 56.0′	–	–	1
3	Guerrero Negro	CICESE	27° 53.0′	114° 09.0′	–	–	1
4	Isla de Cedros	CICESE	28° 05.8′	115° 11.0′	–	–	1
5	La Paz	UNAM	24° 16.0′	110° 20.0′	–	–	1
6	Cabo San Lucas	CICESE	22° 31.7′	109° 32.7′	1	–	–
7	Mazatlan	UNAM	23° 10.9′	106° 25.4′	–	–	1
8	Puerto Vallarta	UNAM	20° 39.5′	105° 14.6′	–	–	1
9	Manzanillo	CICESE	19° 03.8′	104° 17.9′	–	1	1
	Manzanillo	NTWC	19° 01.8′	104° 12.0′	1	–	–
10	Lazaro Cardenas	UNAM	17° 56.4′	102° 10.7′	6	1	1
11	Zihuatanejo	UNAM	17° 38.2′	101° 33.5′	–	1	–
12	Acapulco	UNAM	16° 50.3′	99° 54.2′	6	1	1
	Acapulco	CICESE	16° 50.0′	99° 55.0′	1	–	–
13	Puerto Angel	UNAM	15° 40.0′	96° 29.5′	–	–	1
14	Huatulco	UNAM	15° 45.2′	96° 7.8′	–	1	1
15	Salina Cruz	UNAM	16° 19.1′	95° 11.8′	6	–	1
16	Puerto Madero	UNAM	14° 42.7′	92° 24.1′	6	–	–
	Puerto Madero	NTWC	14° 41.8′	92° 24.7′	–	–	1
17	DART 46412 (3770 m)	NCEI/NDBC	32° 27.9′	120° 34.5′	0.25	1[a]	–
18	DART 43412 (3065 m)	NDBC	16° 01.6′	106° 59.8′	1[a]	1[a]	1[a]
19	DART 43413 (3560 m)	NCEI/NDBC	10° 50.5′	100° 08.2′	0.25	1[a]	1[a]
20	DART 46411 (4334 m)	NCEI/NDBC	39° 20.0′	127° 04.9′	–	0.25	0.25
21	DART 51407 (4738 m)	NCEI/NDBC	19° 33.2′	156° 32.7′	–	0.25	–
22	DART 51406 (4450 m)	NCEI/NDBC	8° 28.4′[a]	125° 01.6′	–	0.25	–

UNAM Institute of Geophysics, National Autonomous University of Mexico, *CICESE* Center for Scientific Research and Higher Education, Mexico, *NTWC* National Tsunami Warning Center, Palmer, Alaska, USA, *NCEI* National Centers for Environmental Information, NOAA, Boulder, Colorado, USA, *NDBC* National Data Buoy Center, NOAA, Stennis Space Center, Mississippi, USA

[a] "Event mode" DART data

The event-mode data were used only to estimate specific statistical parameters of the tsunami waves in the open ocean (in particular, arrival times) and for comparison of these parameters with similar parameters from the coastal observations. The 15-s data were used for a broad range of analyses on open-ocean tsunami properties, including spectral analysis and evaluation of tsunami energy. The DART data were obtained from the National Centers for Environmental Information (NCEI), NOAA, Boulder, Colorado and the National Data Buoy Center (NDBC), NOAA, Stennis Space Center, Mississippi.

There were three DART stations operating near the coast of Mexico from 2010 to 2015: 46412, 43412 and 43413 (Fig. 3). Two of these stations, 46412 and 43413 (Fig. 2a), were retrieved and re-installed in 2011. The data from these stations for the 2010 event were downloaded and thoroughly examined (these data were also used by Rabinovich et al. 2013a, b; Eblé et al. 2015 to examine the energy decay and the effect of the leading negative phase). Unfortunately, no corresponding data from DARTs located in close proximity to the Mexican coast were available for 2014 and 2015. That is why, to investigate the spectral characteristics of the 2014 and 2015 tsunamis, we had to use other DART stations located in the southeastern part of the North Pacific, which had available 15-s downloaded data: 46411, 51406 and 51407 for the 2014 tsunami (Fig. 2b) and 46411 for the 2015 tsunami (Fig. 2c). Boiler-plate information for these stations is included into Table 1.

The digital records from all coastal and open-ocean stations have been examined using the data analysis procedures and tsunami detection methods described by Rabinovich et al. (2006, 2013a), Thomson et al. (2007) and Stephenson and Rabinovich (2009). We verified all data and then corrected any errors, filled gaps and fixed spikes. The tides were calculated by the least squares method (cf. Parker 2007) and subtracted from the original records; the corresponding residual time series were used in all subsequent analysis. To suppress low-frequency sea level fluctuations, mainly associated with atmospheric processes, and to simplify tsunami detection, we high-pass filtered the de-tided time series using a 3-h Kaiser-Bessel (KB) window (cf. Thomson and Emery 2014). These filtered series were then used to construct plots of tsunami records for various sites and to estimate statistical characteristics of the waves. To examine the spectral properties of the tsunami oscillations, we used the unfiltered residual time series.

3. *The Chile (Maule) Tsunami of 27 February 2010*

The Chile (Maule) M_w 8.8 thrust-fault earthquake occurred at 03:34 Local Chilean Time (06:34 UTC) on 27 February 2010 near the coast of Central Chile on the interface between the Nazca and South American plates. The epicenter of the earthquake (35.91°S; 72.33°W; 35 km depth) was located offshore from the Maule region. The source area of the 2010 Chilean earthquake—which was about 550 km long, more than 100 km wide and covered an area of approximately 82,500 km^2 (Pararas-Carayannis 2010; Delouis and Nocquet 2010; Tong 2010)—was situated immediately to the north of the rupture zone of the M_w 9.5 Great Chilean Earthquake of 22 May 1960 (Fig. 1). The 2010 earthquake was one of the most powerful earthquakes in human history and the largest in the Southern Hemisphere since 1960. The earthquake generated a trans-oceanic tsunami (Fig. 2a) that caused a major damage and loss of life along 800 km of the Central Chilean coast and at a number of Chilean islands; the maximum observed tsunami run-up was 29 m (Fritz et al. 2011). Tsunami alerts (Warnings and Advisories) were declared for 54 Pacific countries, including Mexico, the United States, Canada, Russia and Japan (Pararas-Carayannis 2010). Although tsunami waves were observed throughout the entire Pacific Ocean, no noticeable damage or casualties were reported, except for Chile and California (Fritz et al. 2011; Wilson et al. 2010, 2013).

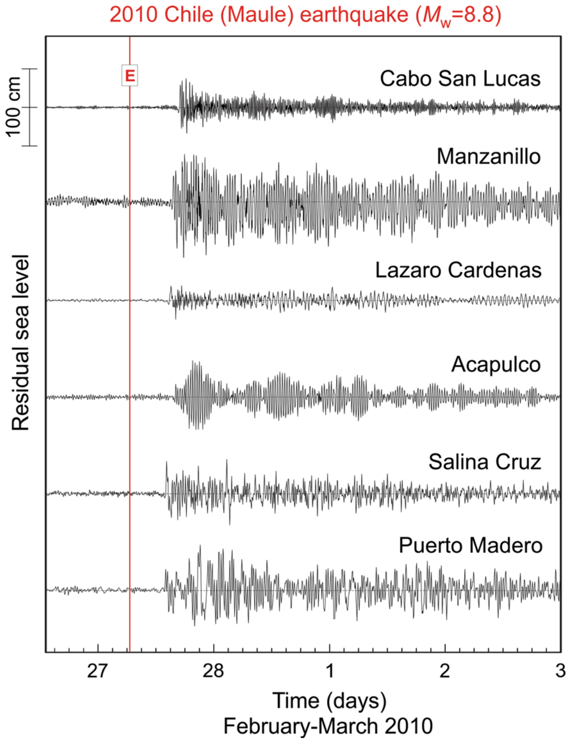

Figure 4
The 27 February 2010 Chilean tsunami recorded by tide gauges at six sites on the coast of Mexico. Time series are the residual sea levels obtained by removing the calculated tides from the original time series and then high-pass filtering the resulting de-tided time series with a 3-h Kaiser–Bessel window. The *solid vertical red line* labelled "E" denotes the time of the earthquake

3.1. *Tsunami Observations*

The 2010 tsunami waves on the Pacific coast of Mexico were recorded by all seven coastal tide gauges in operation at the time of event (Figs. 4, 5). The tide gauges were located at six sites, including two independent instruments at Acapulco, one with 1-min sampling and one with 6-min sampling. The principal parameters of the observed tsunamis are

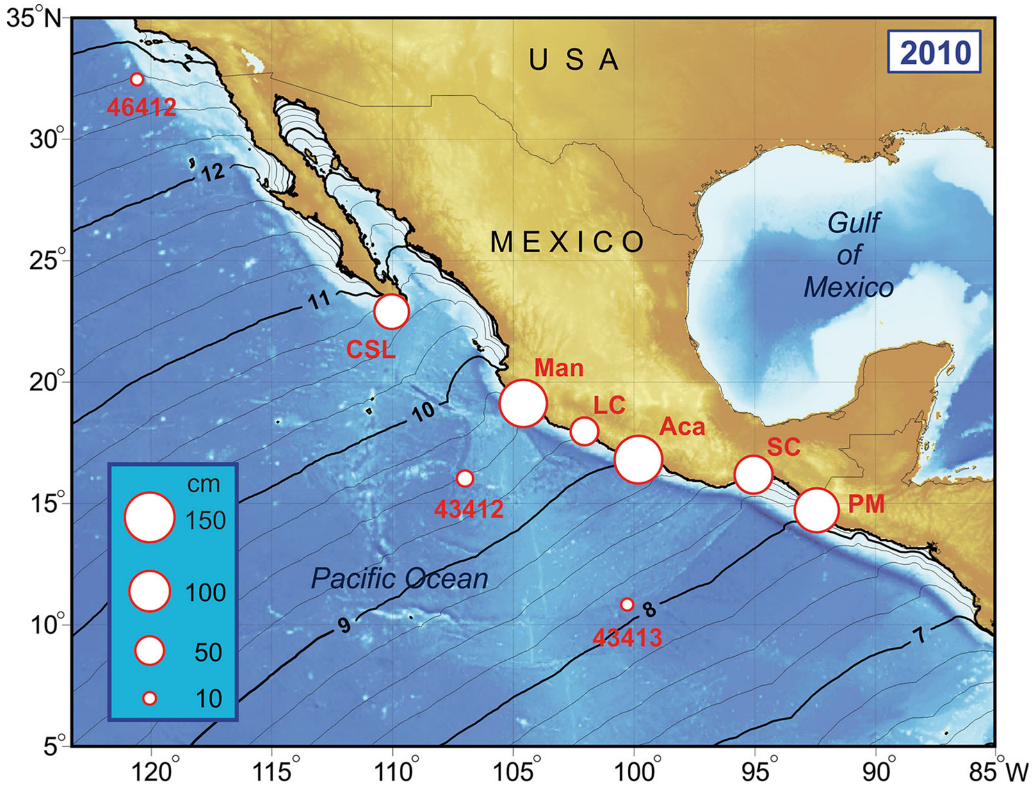

Figure 5
Map of coastal Mexico showing the tide gauge sites and the three offshore DART stations that recorded the 27 February 2010 Chile tsunami (*white circles*). The size of a circle is proportional to the maximum recorded trough-to-crest wave height. The abbreviated names are: *CSL* Cabo San Lucas, *Man* Manzanillo, *LC* Lazaro Cardenas, *Aca* Acapulco, *SC* Salina Cruz, and *PM* Puerto Madero. *Black solid lines* show the 2010 tsunami travel time (in hours and 15 min) from the source area computed using the wavefront orientation method (Fine and Thomson 2013)

given in Table 2. The parameters estimated for the two Acapulco tide gauges were in close agreement, except that the wave heights recorded by the UNAM (6-min) gauge were approximately 30–35 % smaller than those recorded by the CICESE (1-min) gauge. Candella et al. (2008) examined the influence of sampling interval on measured tsunami wave heights and demonstrated that it can be considerable, especially for high-frequency events. However, even low-frequency tsunami heights are attenuated when recorded at long sampling intervals; for example, the maximum 2004 Sumatra tsunami height at Manzanillo (Mexico) recorded with a 6-min sampling was 89 cm (Rabinovich et al. 2006), while a maximum wave height of 101 cm was obtained from a 2-min record found some time later (Rabinovich et al. 2011).

We inspected the tsunami records and estimated statistical parameters of the tsunami waves, including visual periods of the measured waves (Table 2). The observed travel times of the arriving waves were compared with travel times computed by the "*wave-front orientation method*" (Fine and Thomson 2013), which is more accurate and computationally efficient than the conventional multiple grid-point method. We found several important features of the observed 2010 tsunami waves on the coast of Mexico (Table 2; Figs. 4, 5):

1. The tsunami waves were clearly recorded along the entire Pacific coast of Mexico. The highest trough-to-crest wave heights were observed at Acapulco (138 cm), Manzanillo (134 cm) and Puerto Madero (116 cm); surprisingly, the lowest

Table 2

Parameters of the Chilean tsunami of 27 February 2010 recorded on the coast of Mexico (Main shock, M_w 8.8 at 06:34 UTC)

Station	Sampling (min)	First wave			Maximum waves			Observed tsunami variance (cm^2)	Visually estimated period (min)
		Arrival time (UTC)	Travel time (hh:mm)	Amplitude (cm) Sign	Amplitude (cm)	Time (UTC) of max amplitude	Wave height (cm)		
Cabo San Lucas	1	17:29	10:55	+38	42	18:33	72	61.7	11
Manzanillo	1	16:34	10:00	+37	63	19:04	134	647.4	28
Lazaro Cardenas	6	16:09	09:35	+22	22	16:30	46	45.1	24, 60
Acapulco 1	6	15:51	09:17	+21	45	19:30	87	322.9	27
Acapulco 2	1	15:50	09:16	+31	65	19:30	138	258.9	27
Salina Cruz	6	15:57	09:23	+42	42	4:30[a]	86	178.9	30
Puerto Madero	6	15:45	09:11	+26	60	23:06	116	429.8	30
DART 46412	0.25	19:33	12:59	+12	12	19:43	13	2.01	13
DART 43412	1[b]	16:12	09:38	+14	14	16:23	16	–	8
DART 43413	0.25	14:45	08:11	+8	8	14:56	9	1.87	6, 8

All times are in UTC for 27 February 2010, except where indicated

[a] 28 February 2010

[b] Event mode data

wave heights occurred at Lazaro Cardenas (up to 46 cm) located between Acapulco and Manzanillo (Fig. 5). The relatively small tsunami signal at Lazaro Cardenas station is probably due to effects of the local slope topography and location of the tide gauge at the far side of the semi-enclosed Lazaro Cardenas harbour.

2. The UNAM tide gauge (6-min) at Acapulco had a maximum wave height of 87 cm, which is in close agreement with official maximum of 90 cm reported on the National Mareographic Service of Mexico website. This height was significantly smaller than the 138 cm reported for the CICESE (1-min) gauge.
3. The 2010 tsunami waves were first recorded at 15:45 UTC at Puerto Madero, the southernmost Mexican tide gauge station, and then at other stations. Finally, at 17:29 UTC the waves arrived at Cabo San Lucas at the southern end of the Baja California Peninsula. The respective travel times of 9 h 11 min and 10 h 55 min after the main shock are in good agreement with numerically estimated tsunami travel times (Fig. 5).
4. The periods of the recorded waves were fairly consistent: 24–30 min at all stations except Cabo San Lucas where relatively high-frequency oscillations (11 min) were observed.
5. Maximum wave amplitudes at most sites were observed several hours after the first wave arrival: from 2.5 h at Manzanillo to 12.5 h at Salina Cruz.[2] The two exceptions are Lazaro Cardenas, where the maximum wave was the first wave, and Cabo San Lucas, where the fourth wave was the highest (~1 h after the first wave arrival).
6. The signal-to-noise (s/n) ratio was high at all stations; consequently the first tsunami arrival was well defined. The leading wave at all sites was *positive* (“crest wave”).
7. The tsunami ringing at all stations was quite long, lasting for 4–5 days, similar to that observed on the coast of British Columbia (BC), Canada (Rabinovich et al. 2013a) and the Kuril Islands, Russia (Shevchenko et al. 2013). The ringing time is also comparable to that observed on the coast of California after the 1960 Chile tsunami (Miller et al. 1962). Slow energy decay at the Mexican stations is in good agreement with the results of Rabinovich et al. (2013b) who, based on the analysis of 23 open-ocean DART records, estimated the mean decay (*e*-folding) time for the 2010 Chile tsunami to be approximately 25 h.

---

[2] The first wave at Salina Cruz was also quite strong, but slightly weaker than the wave that arrived after 12.5 h (Fig. 4).

The mean tsunami wave height for the Mexican coast, averaged over 7 records, is 98.7 cm. We also used 34-h tsunami segments to evaluate the "observed tsunami variance" (see the corresponding column in Table 2). Maximum variance was at Manzanillo (647 cm^2) and at Puerto Madero (430 cm^2); mean variance (Var_0) averaged over all records is $\sim$278 cm^2. The estimates of maximum wave heights and tsunami variance clearly show that there are "*hot spots*" (Manzanillo, Puerto Madero and Acapulco), where tsunami waves are considerably higher than the mean. In contrast, at some other stations, e.g., at Cabo San Lucas and Lazaro Cardenas, the waves are relatively small.

To examine the 2010 tsunami wave properties seaward of the Mexican coast, we used the open-ocean BPR (DART) stations (Table 1). Because they are not affected by the coast and have very low background noise compared to the coastal tide gauges, deep-water BPRs provide the most accurate and precise information about tsunami waves (cf., Titov 2009; Thomson et al. 2011). For two DARTs, 46412 and 43413, we took advantage of long, high-quality 15-s data downloaded from the retrieved instruments; for DART 43412 a few hours of the 1-min event-mode data (see Mungov et al. 2013 for details of DART operations) were used. The DART records of the 2010 tsunami waves (Fig. 6) demonstrate obvious similarities for waves observed at open-ocean stations, similarities that are entirely absent in the coastal tsunami records (Fig. 4).

In general, the findings based on the open-ocean tsunami observations are in close agreement with the results from the coastal measurements and with the theoretically computed travel times shown in Fig. 5. The actual arrival times at DART stations match well with the Estimated Times of Arrival (ETA) evaluated by the National Tsunami Warning Center (NTWC, Palmer, AK): 14:40 (DART 43413), 16:05 (43412) and 19:20 (46412). The differences from our estimates (Table 2) are only a few minutes. At all three DART stations near the Mexican coast, the first wave had the maximum amplitude; the leading semi-wave was positive and, for open-ocean records, was quite high: 9–16 cm. The ETA estimates from DART measurements and numerical computations (Table 2; Fig. 5) show that the tsunami waves propagated in the northwest direction along the continental margin of Mexico for almost 5 h.

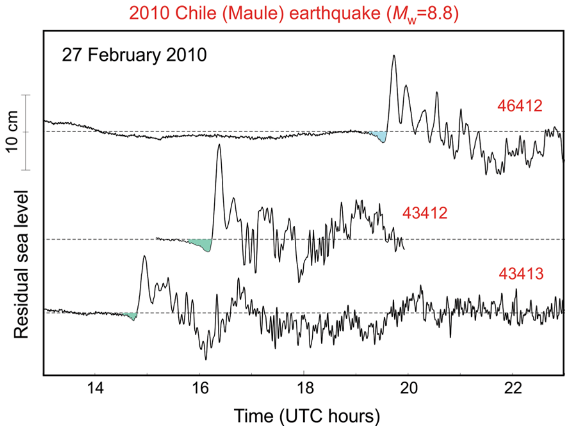

Figure 6
The 27 February 2010 Chilean tsunami recorded by three DARTs offshore from the coast of Mexico. The records are de-tided but unfiltered. The *light blue shaded areas* are the "negative phase" of the open-ocean tsunami records associated with subsidence of Earth's crust under the tsunami wave loading

A principal feature of the 2010 DART records is the relatively small (1.0–1.5 cm) trough that preceded the major frontal crest wave (Fig. 6). It is important to note that records shown in Fig. 6 are *unfiltered*, i.e., that this is a natural effect and not artificially induced by record filtering. A similar feature was found by Rabinovich et al. (2013a) in the BC coastal and offshore records for the 2010 Chile tsunami and in a great number of DART records throughout the Pacific Ocean. Watada et al. (2014) attribute the negative trough to the elasticity of the solid earth and to the additional effects of seawater compressibility and gravitational potential changes associated with mass motion during tsunami propagation. Eblé et al. (2015) examined open-ocean and coastal records of four major tsunamis (2010 and 2014 Chile, 2011 Tohoku and 2012 Haida Gwaii) and found a negative leading trough in most of the records; the effect became stronger with increasing distance from the source region. A small trough that preceded the leading wave crest is also detectable in some coastal records examined in this study, in particular for Acapulco, Cabo San Lucas and Lazaro Cardenas (Fig. 4), but high background noise level prevented us from providing a detailed examination of this effect.

3.2. Spectral Analysis

Sea level oscillations observed near the coast during a tsunami may be represented as

$$\zeta_{\mathrm{obs}}(t) = \zeta_{\mathrm{tsu}}(t) + \zeta_{bg}(t), \tag{1}$$

where ζ_{tsu} is the height of tsunami waves generated by an underwater seismic source, ζ_{bg} is the height of background long-wave oscillations and t is time. The observed spectrum $S_{\mathrm{obs}}(\omega)$ then has the form

$$S_{\mathrm{obs}}(\omega) = S_{\mathrm{tsu}}(\omega) + S_{bg}(\omega), \tag{2}$$

where ω is the angular frequency and $S_{\mathrm{tsu}}(\omega)$ and $S_{bg}(\omega)$ are the tsunami and background spectra, respectively. In practice, we do not know the exact background spectrum, $S_{\mathrm{bg}-t}(\omega)$, *during the event,* but we can assume that it is approximately the same as *before the event* (i.e., at $t = 0$), whereby

$$S_{\mathrm{bg}-t}(\omega) \approx S_{\mathrm{bg}-0}(\omega) = S_{\mathrm{bg}}(\omega). \tag{3}$$

To examine the spectral properties of tsunami oscillations during the 27 February 2010 Chile tsunami and to compare these properties with those of the background oscillations at the same sites, we separated the records into two parts based on (3). The time period preceding the tsunami arrivals (5.6 days for the four 6-min stations and 4.6 days for the three 1-min stations) was identified as "normal" and selected for analysis of the background signals. For the "tsunami" periods following the wave arrivals, we chose time periods of 32 and 34 h for these two groups of stations, respectively. Our spectral analysis procedure is similar to that described by Thomson and Emery (2014) (see also, Rabinovich et al. 2013a). To improve the spectral estimates, we used a Kaiser-Bessel (KB) spectral window with half-window overlaps prior to the Fourier transform. The length of the window was chosen to be $N = 128$ (768 min) for 6-min records and $N = 512$ min for 1-min records, yielding $\nu = 40$ (50) degrees of freedom for the background spectra and $\nu = 8$ (14) for the tsunami spectra; the spectral resolution is $\Delta f \approx 0.78$ (0.117) cph and the Nyquist frequency $f_n = 5$ (30) cph for 6-min (1-min) records. The computed tsunami and background spectra for six coastal sites are shown in Fig. 7 (for Acapulco the spectra of the 6-min and 1-min records are combined).

In general, the spectra for both the tsunami and background records are "red",[3] with spectral energy decreasing with increasing frequency. At most stations, the difference between the tsunami and background spectra is considerable, demonstrating that the 2010 Chile tsunami was quite strong. The spectral peaks differ at each station, showing the substantial influence of local topographic effects. The most prominent peaks are observed at Cabo San Lucas (periods of about 10.5 and 5 min), Manzanillo (27 min), Lazaro Cardenas (51 and 16 min) and Acapulco (27 min), which are the same for tsunami and background spectra, indicating the resonance nature of the tsunami peaks. This result is in good agreement with the well-known finding that tsunami wave periods recorded at the coast are closely related to the resonant properties of the local/regional topography rather than to characteristics of the tsunami source, and are almost the same as those of long background sea level oscillations (such as seiches) for the same sites. For this reason, the spectra of tsunamis from different earthquakes are usually similar at the same location, while the spectral peaks for the same event are significantly different at different locations (cf. Honda et al. 1908; Miller et al. 1962; Miller 1972).

3.3. Spectral Ratios (Source Functions)

Because of the dominant influence of local topography on arriving tsunami waves, it is difficult to reconstruct the spectral characteristics of the source region based on the data from coastal tide gauges. Rabinovich (1997) suggested a method to bypass this problem and separate the influences of the topography and the source on the observed tsunami spectrum. The method is based on the assumption that the transfer function, $W(\omega)$, describing the linear topographically induced transformation of long waves approaching the coast, is the same for tsunami

---

[3] This is a typical definition in spectral analysis. In analogy with light, a "red spectrum" is one in which energy is mainly at low frequencies and decreases with increasing frequency; a "blue spectrum" has most energy at high frequencies and energy increases with increasing frequency. A "white spectrum" has uniform energy distribution (cf. Thomson and Emery 2014).

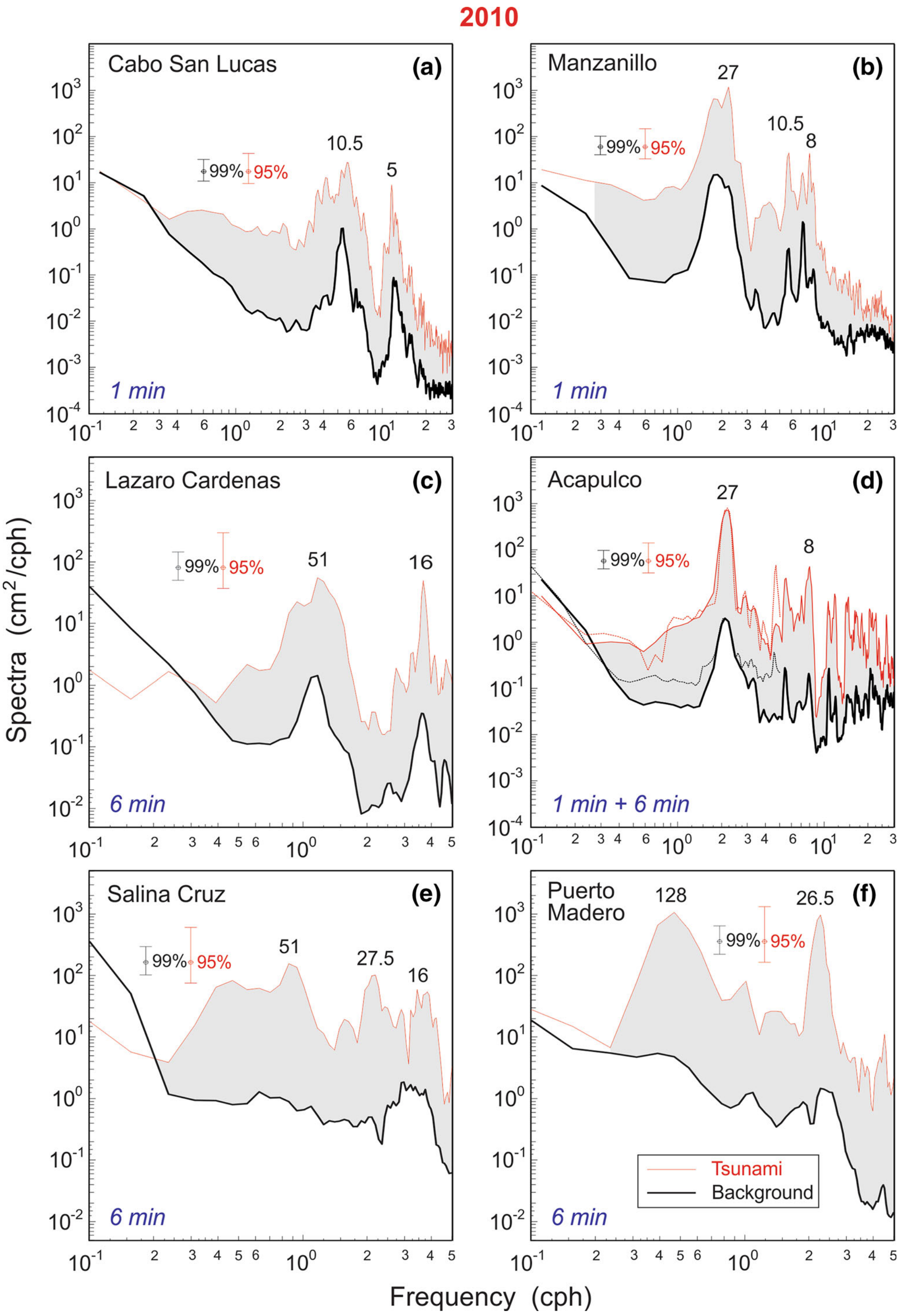

Figure 7

Spectra of background (pre-tsunami) and 2010 tsunami sea level oscillations for seven tide gauge records from the coast of Mexico. For Acapulco, both spectra of UNAM (6 min) and CICESE (1 min) records are shown in the same plot. Periods (in min) of the main spectral peaks are indicated. The 95 % confidence level applies to the tsunami spectra, the 99 % confidence level to the background spectra. The *shaded areas* denote the tsunami energy waves and the ever-present background long waves. Specifically,

$$S^j_{\rm tsu}(\omega) = W_j(\omega)\, E^j_{\rm tsu}(\omega); \tag{4a}$$

$$S^j_{bg}(\omega) = W_j(\omega)\, E^j_0(\omega), \tag{4b}$$

where $S^j_{\rm tsu}(\omega)$ and $S^j_{\rm bg}(\omega)$ are the tsunami and background spectra at the jth site, $E^j_{\rm tsu}(\omega)$ and $E^j_0(\omega)$ are the tsunami and background spectra in the open ocean, respectively. Using (4a), we next assume that all distinct characteristics of the observed spectra at the jth site are related to the site-specific topographic function, $W_j(\omega)$, while all general properties of these spectra are associated with the tsunami source. In other words, we assume that the function $W_j(\omega)$ is strongly variable in space (due to the resonant properties associated with the local bathymetry and basin dimensions) but almost constant in time. Conversely, the corresponding source function $E^j_{\rm tsu}(\omega)$ is spatially uniform, $E^j_{\rm tsu}(\omega) \approx E_{\rm tsu}(\omega)$, but varies considerably with time depending on the actual source parameters. Also, from numerous observations in the open ocean (cf. Kulikov et al. 1983; Filloux et al. 1991; Rabinovich and Eblé 2015), we know that background spectra in the open ocean, $E^j_0(\omega)$, are spatially and temporarily highly similar, whereby $E^j_0(\omega) \approx E_0(\omega)$.

The ratio,

$$R^j_s(\omega) = S^j_{\rm tsu}(\omega)/S^j_{\rm bg}(\omega), \tag{5}$$

of the tsunami to the background spectrum suppresses the local topographic influence, thereby enabling us to obtain a function that is determined almost solely by the external forcing (i.e., by the characteristics of the open ocean tsunami waves). Although the true tsunami spectrum at the coast, $S^j_{\rm tsu}(\omega)$, is unknown, we know the observed coastal spectrum, $S^j_{\rm obs}(\omega)$, for sea level oscillations formed by the superposition of tsunami waves and background noise. Taking into account (2), (3) and (4a, 4b), we can specify the "spectral source function"[4] that quantifies the amplification of the long-wave spectrum due to the tsunami event relative to the background conditions:

$$R_j(\omega) = \frac{S^j_{\rm obs}(\omega)}{S^j_{\rm bg}(\omega)} = \frac{\left[E^j_{\rm tsu}(\omega) + E^j_0(\omega)\right]}{\hat{E}^j_0(\omega)} \approx R^j_s(\omega) + 1.0, \tag{6}$$

where according to (3) the open-ocean background spectrum before and during the event are approximately equal: $\hat{E}^j_0(\omega) \approx E^j_0(\omega)$. For each tsunami event, the individual spectral ratio function at the jth site, $R_j(\omega)$, is an invariant characteristic of the source and is, therefore, expected to be similar at all stations. The similarity of the function $R_j(\omega)$ at various stations validates our initial assumptions. In fact, the high efficiency of this method has been demonstrated for many tsunami events (cf. Rabinovich 1997; Vich and Monserrat 2009; Shevchenko et al. 2013; Rabinovich et al. 2013a, b).

Figure 8 presents the spectral ratios (proxy source functions) for seven spectra derived from the tide gauge spectra shown in Fig. 7. In contrast to the individual spectra, which are markedly different and have specific resonant peaks, the source functions for the various sites are much more similar and have no specific peaks related to coastal topographic resonance (i.e., those individual peaks which were observed in the coastal spectra). In general, the source functions have a characteristic "bulge-like" shape spanning a broad frequency band from about 0.25–30 cph (periods from 4 h to 2 min). For the 2010 Chilean tsunami, the maximum source functions (i.e., maximum amplification of the tsunami waves relative to the background noise) occurred at frequencies of 1–10 cph (periods from 60 to 6 min). The most interesting common feature of $R_j(\omega)$ observed at all sites, except Lazaro Cardenas, is a peak with period at about 27 min (denoted by a dashed red line in Fig. 8). A similar peak period (26 min) was found by Rabinovich et al. (2013a) in the spectral ratios ("source functions") for all coastal and open-ocean stations in the area of British Columbia. Moreover, the dominant 26 min peak was found by Rabinovich et al. (2013b) in the spectral ratios for available DART records for the 2010 Chilean tsunami throughout the Pacific Ocean. Also, this particular peak was identified by Shevchenko et al. (2013) in spectra and spectral ratios of the 2010 tsunami records from DARTs 21416 and 21419 located near the Kuril Islands. It appears that

---

[4] We qualify this by noting that the "source function" can be indicative not only of the initial seismic source but also of secondary remote sources associated with open ocean tsunami wave scattering and reflection.

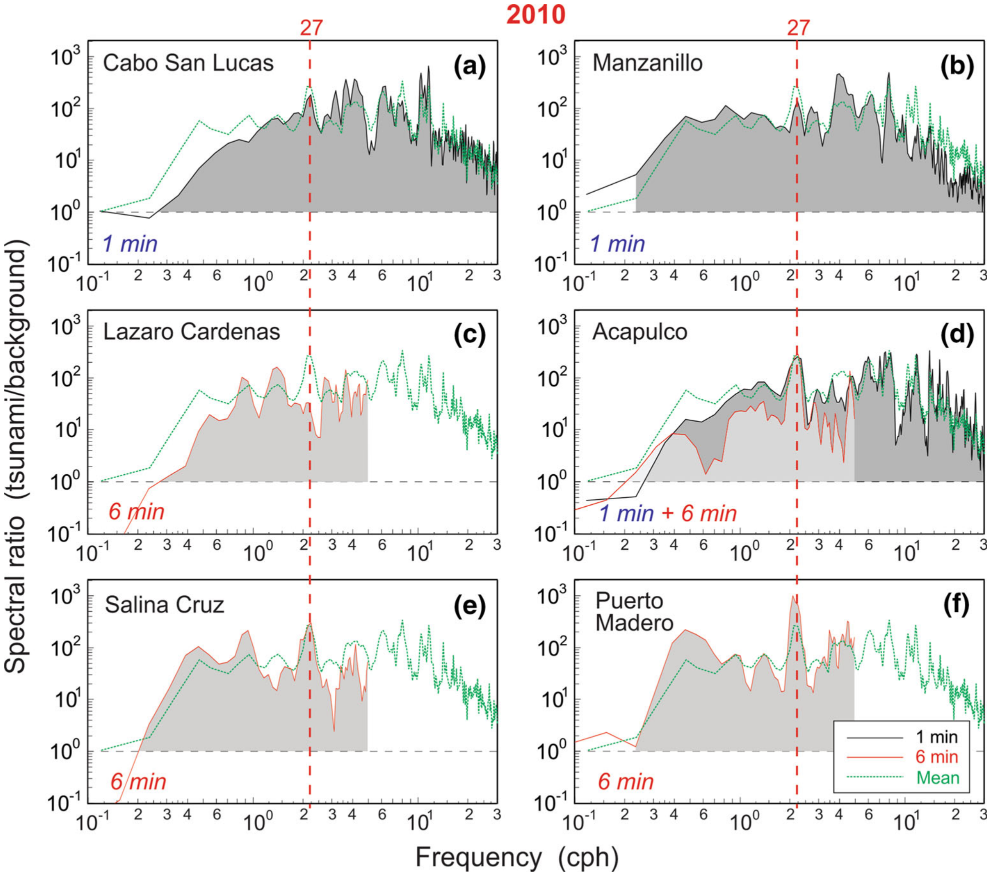

Figure 8

Computed tsunami/background spectral ratios for the seven coastal tide gauge spectra shown in Fig. 7. *Shaded areas* denote the tsunami response associated with the arriving waves; i.e., the amplification of the spectra due to the tsunami waves, measured relative to the background spectra. The *green solid line* shows the mean spectral ratio estimated by averaging seven individual spectral ratios. The *dashed vertical red line* indicates the period of 27 min

this consistent wave property is related to a specific feature of the original source region of the 2010 tsunami.

4. The Chile (Iquique) Tsunami of 1 April 2014

The Chile (Iquique) M_w 8.2 interplate thrust earthquake occurred at 20:46:47 Local Chilean Time (23:46:47 UTC) on 1 April 2014 in the subduction zone off the coast of northern Chile (Lay et al. 2014). The epicenter of the earthquake (19.61°S; 70.769°W; 23 km depth) was located offshore 70 km north of Iquique, approximately 1600 km north from the epicenter of the 2010 earthquake (Fig. 1). The source area of the 2014 Chilean earthquake was compact, about 100 km long, 40 km wide and covered an area of approximately 4000 km^2 (Gusman et al. 2015). The earthquake occurred in the area that had been considered an important seismic gap: the last strong earthquake in this area was the great 1877 Tarapaca Earthquake (M_w 8.8–9.0) (Kulikov et al. 2005; Calisto et al. 2015). The earthquake generated a moderate trans-oceanic tsunami (cf. An et al. 2014; Heidarzadeh et al. 2015). According to a post-tsunami field survey, the 2014 event was characterized by a relatively uniform distribution of run-up heights of 2–3 m, with a maximum height of 4.6 m at sites closest to the earthquake epicenter (Catalán et al. 2015). Although tsunami waves were observed

Table 3

Parameters of the Chilean tsunami of 1 April 2014 recorded on the coast of Mexico (Main shock, M_w 8.2 at 23:47 UTC)

Station	Sampling (min)	First wave			Maximum waves			Observed tsunami variance (cm^2)	Visually estimated period (min)
		Arrival time (UTC)	Travel time (hh:mm)	Amplitude (cm) Sign	Amplitude (cm)	Time (UTC) of max amplitude	Wave height (cm)		
Ensenada	1	11:35	11:48	+4	18	22:35	36	22.8	25
Manzanillo	1	?	?	?	18	7:17[a]	37	48.9	27
Lazaro Cardenas	1	8:11	08:24	+3	7	12:45	15	4.1	16
Zihuatanejo	1	7:49	08:02	+6	23	15:08	43	64.2	15, 20
Acapulco	1	7:18	07:31	+10	22	14:07	36	34.2	31
Huatulco	1	7:00	07:13	+6	15	19:28	29	22.2	14
DART 46412	1[b]	11:19	11:32	+1.1	1.1	11:31	1.6	–	22
DART 43412	1[b]	7:53	08:06	+1.1	1.1	8:02	1.6	–	8, 23
DART 43413	1[b]	6:26	06:39	+0.9	0.9	6:34	1.6	–	8, 21

All times are in UTC on 2 April 2014, except where indicated

[a] 3 April 2014

[b] Event mode data

throughout the entire Pacific Ocean, no noticeable damage was reported (Omira et al. 2016). Nevertheless, the event was the subject of considerable scientific interest and study (cf. An et al. 2014; Heidarzadeh et al. 2015; Eblé et al. 2015; Gusman et al. 2015; Calisto et al. 2015).

4.1. *Tsunami Observations*

The 2014 tsunami waves were recorded by several tide gauges on the Pacific coast of Mexico. Here, we examine six available coastal records of the event (Table 3; Figs. 9, 10). The sampling interval for all records was 1 min. Tsunami waves reaching the Mexican coast during the 2014 event were much weaker than for the 2010 tsunami, and the s/n ratio was much smaller. As a result, determination of the principal parameters of the observed waves (Table 3), especially the exact tsunami arrival times, was considerably more difficult and sometimes even impossible.

The salient features of the measured 2014 tsunami waves on the coast of Mexico were the following (Table 3; Fig. 9):

1. The tsunami waves were recorded along the entire Pacific coast of Mexico. The highest trough-to-crest wave heights were observed at Zihuatanejo (43 cm). Wave heights at Ensenada, Manzanillo and Acapulco were almost the same (36–37 cm) and, as with the 2010 event, the lowest wave heights occurred at Lazaro Cardenas (15 cm). In

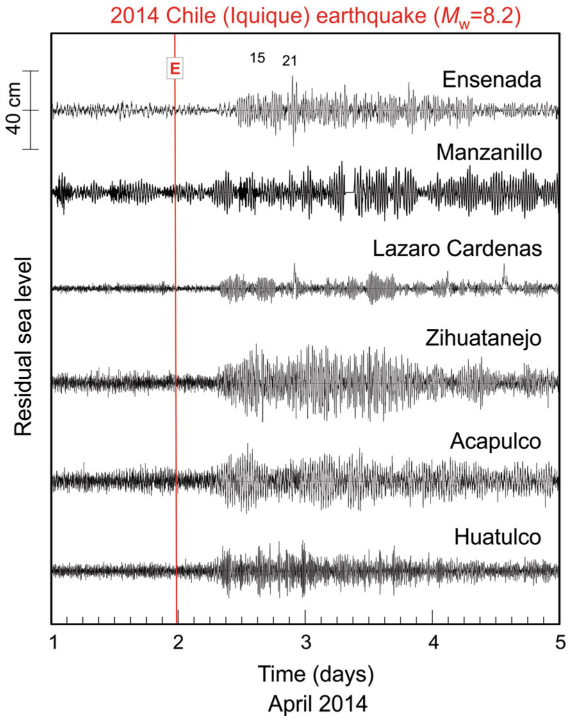

Figure 9
As in Fig. 4 but for the six coastal tide gauge records of the 1 April 2014 Chilean tsunami

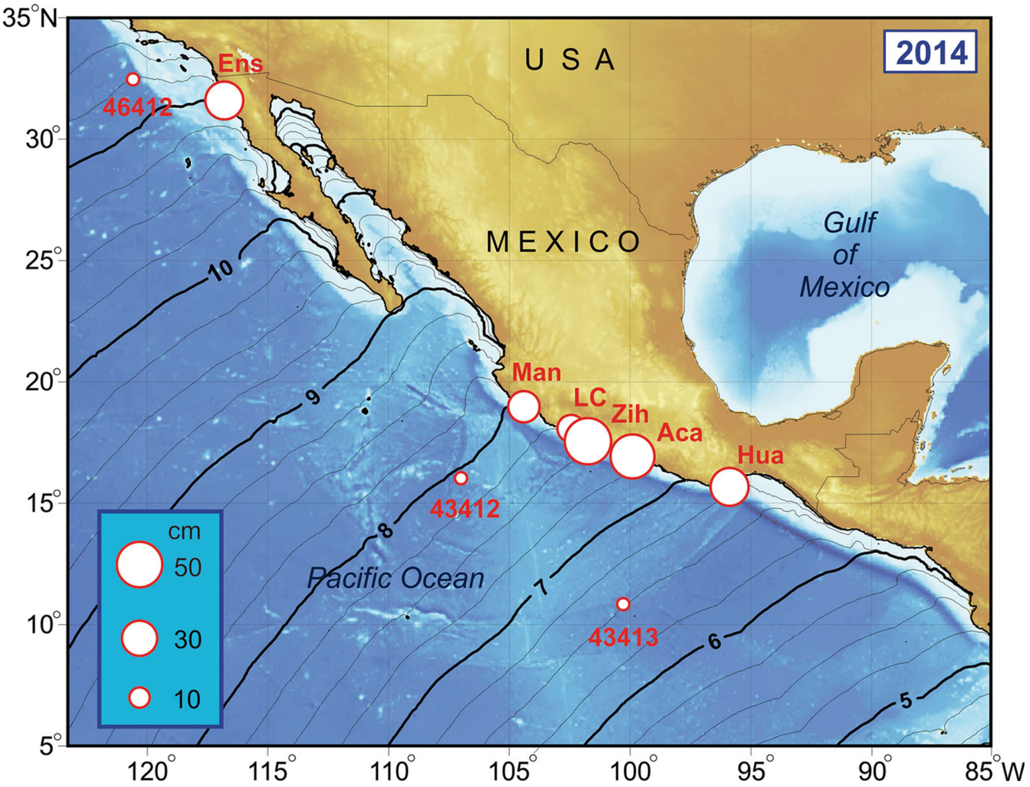

Figure 10

As in Fig. 5 but for the six coastal tide gauges and three DARTs that recorded the 2014 Chilean tsunami. The abbreviated names are: *Ens* Ensenada, *Man* Manzanillo, *Zih* Zihuatanejo, *LC* Lazaro Cardenas, *Aca* Acapulco, and *Hua* Huatulco. *Black solid lines* show the 2014 tsunami travel time (in hours and 15 min) from the source area computed using the wavefront orientation method (Fine and Thomson 2013)

general, the observed tsunami wave heights on the Mexican coast for the 2014 event were 3–4 times smaller than for the 2010 event.

2. Waves from the 2014 tsunami first arrived at 7:00 UTC (7 h 13 min after the earthquake) at Huatulco, the southernmost of the six Mexican tide gauge stations that recorded this tsunami. Then, 15–71 min later, the tsunami waves reached Acapulco, Zihuatanejo and Lazaro Cardenas. Finally, at 11:35 UTC (11 h 48 min after the main shock), the waves arrived at Ensenada, the northernmost Mexican station (Fig. 10). The wave travel times were approximately 1 h 30 min shorter than for the 2010 tsunami (Table 2), in agreement with the closer proximity of the source area to the coast of Mexico (Fig. 1). Pronounced atmospherically induced seiches at Manzanillo (Fig. 9) did not allow us to identify the exact arrival time at this station.
3. Visual inspection of the tide gauge records yields dominant wave periods from 14 min at Huatulco to 31 min at Acapulco.
4. Maximum wave amplitudes at most sites were observed from 7 to 22 h after the first tsunami arrival.
5. Similar to the 2010 event, tsunami ringing at all stations was quite long, lasting for several days (Fig. 9).

The mean tsunami wave height averaged over the six sites was 32.7 cm (three times smaller than in 2010); the observed mean tsunami variance was $Var_0 \sim 33\ \mathrm{cm}^2$ (approximately 8.5 times smaller than for the 2010 tsunami). Maximum variance was at Zihuatanejo ($\sim$64 cm^2) and Manzanillo ($\sim$49 cm^2), while the minimum was at Lazaro Cardenas (4 cm^2).

Because data from the DART stations located near the coast of Mexico during the 2014 tsunami

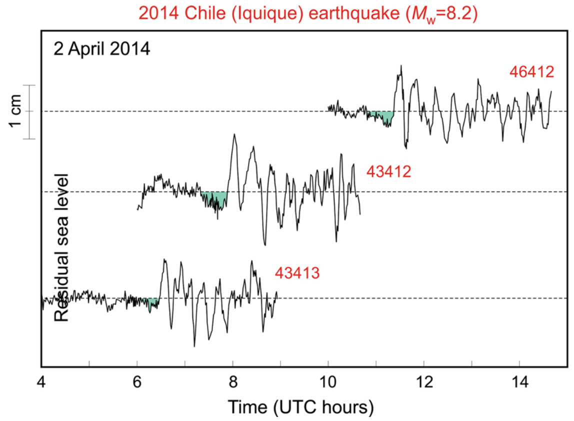

Figure 11
The same as in Fig. 6 but for DART records of the 1 April 2014 Chilean tsunami

(43412, 43413 and 46412) have not been retrieved, there are no 15-s records available for this study. However, we were able to use a few hours of the 1-min event-mode data from these stations to estimate the open-ocean tsunami parameters (Fig. 11; Table 3).

The results from the DART observations are generally in close agreement with those from the coastal measurements; in particular, the tsunami arrival times at the DART stations match well those at the coastal tide gauges. However, these times are significantly delayed relative to the theoretical ETA computed by the NTWC (Palmer, AK): 06:05 UTC (DART 43413), 07:30 UTC (43412) and 10:50 UTC (46412). The differences from the observed values (Table 3) are 21, 23 and 29 min, respectively. These time differences are consistent with the corresponding time delays for the coastal stations relative to the computed times shown in Fig. 10. The reason of the delays relative to the ETAs is unclear. Normally, such delays indicate that the theoretical position of the source area is not quite precise and needs to be corrected (cf. Fine et al. 2015).

There are three specific aspects of the DART tsunami observations that are worth mentioning (Fig. 11): (1) The leading frontal wave at all three sites is distinct and positive and has the *maximum amplitude* (in contrast to the coastal records where the maximum wave occurred several hours after the first arrival); (2) the maximum observed open-ocean wave height for the 2014 tsunami was only 1.6 cm, which compares with wave heights of 9–16 cm in 2010 (Table 2); and (3) similar to the 2010 tsunami (Fig. 6), the leading wave crest was preceded by a small (3–4 mm) but distinct trough, in agreement with the findings of Eblé et al. (2015).

Certainly, the 2014 tsunami was weaker than the 2010 tsunami, as is clearly observed in the tide gauge records (compare Figs. 4 and 9). The coastal waves in 2014 were 3–4 times smaller than in 2010, while the open-ocean waves were eight times smaller (Tables 2, 3). The reason of this difference appears to be related to the character and direction of the energy fluxes for these two events (Fig. 2). It appears that a higher percentage of the tsunami energy for the 2014 event was in the form of coastally trapped tsunami waves (cf. Miller et al. 1962).

4.2. *Spectral Analysis*

Spectral analysis of the six 2014 coastal tide gauge records (Table 3; Fig. 9) was performed in the same manner as for the 2010 event. We used segments of about 4.6 days (6656 min) obtained prior to the tsunami arrival to examine the background spectra and about 34 h of the “tsunami period” (2048 min) to estimate the tsunami spectra. We applied a KB spectral window of $N = 512$ min with half-window overlaps prior to the Fourier transform, yielding $v = 50$ (14) degrees of freedom for the background (tsunami) spectra. The computed spectra are shown in Fig. 12.

The shapes of the tsunami and background spectra are similar to those for the 2010 event. However, in contrast to 2010, the difference between the tsunami and background spectra is noticeably smaller, indicating that the 2014 Chile tsunami was considerably weaker than the 2010 tsunami. The same three tide gauges have been used for the analysis of both 2010 and 2014 events: Manzanillo, Lazaro Cardenas and Acapulco. As expected, the major spectral peaks at these stations for the two tsunamis were similar: Manzanillo, 29 and 8 min (in 2010: 27, 10.5 and 8 min); Lazaro Cardenas, 57 and 15 min (in 2010: 51 and 16 min); and Acapulco, 27 min (in 2010: 27 min). It is obvious that these

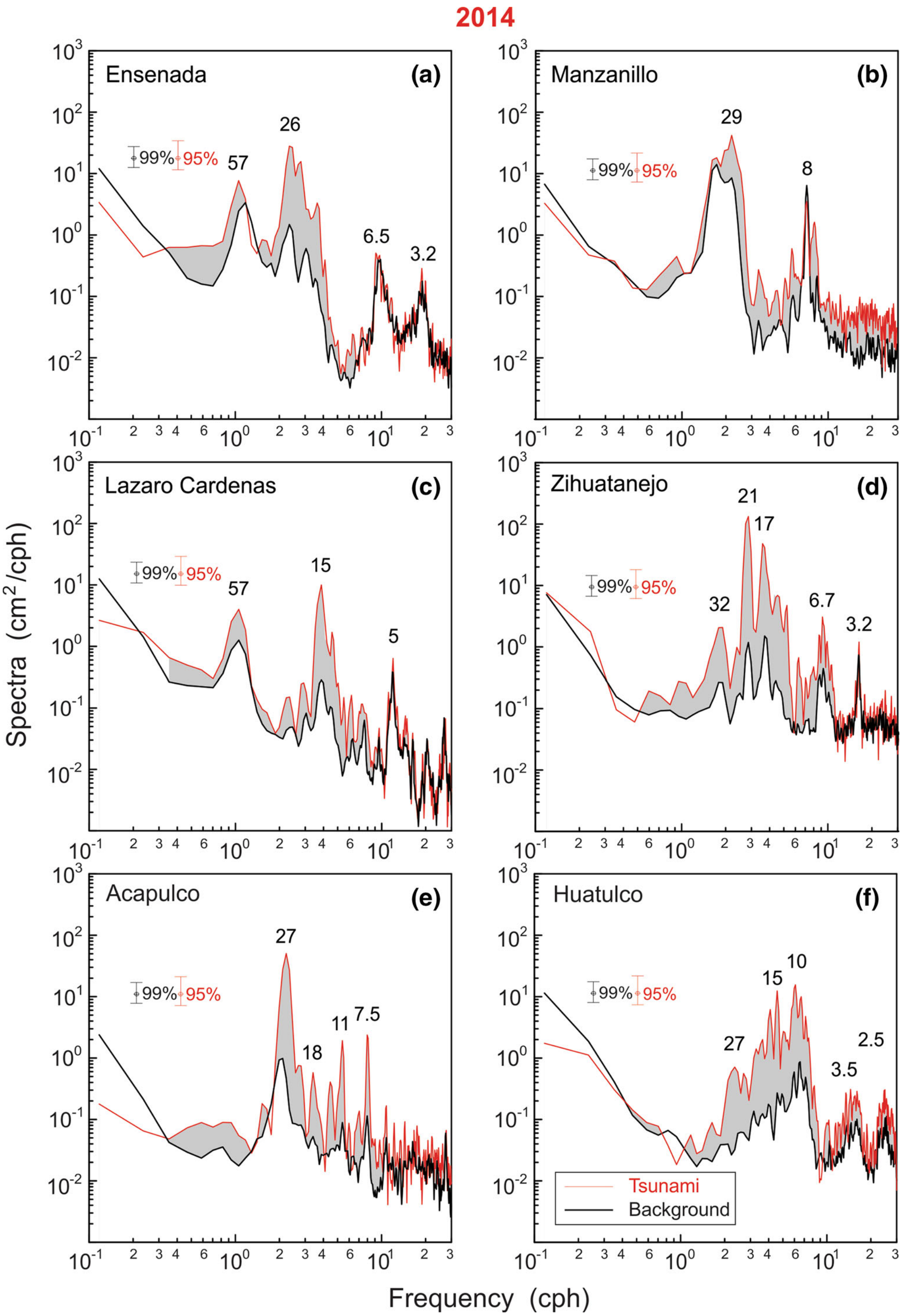

Figure 12
As in Fig. 7 but for the 2014 spectra

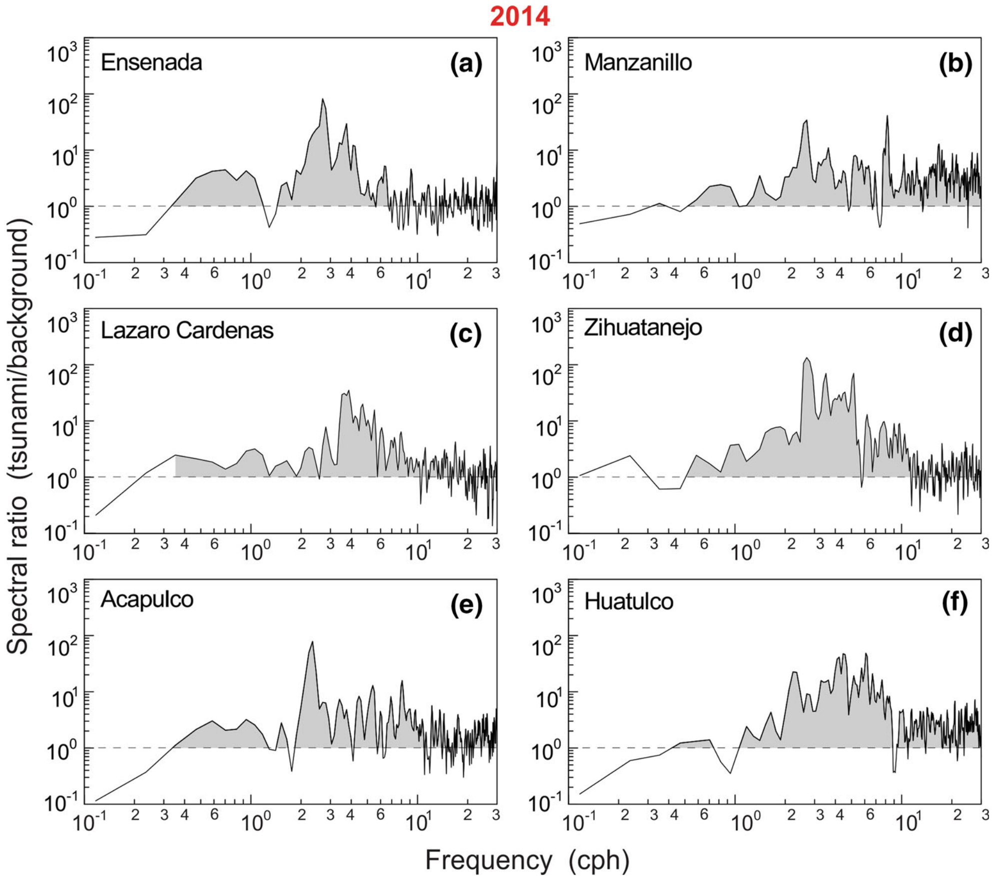

Figure 13
As in Fig. 8 but for the six 2014 spectra shown in Fig. 12

peaks are determined by local topographic effects rather than by the source characteristics.

The most prominent peaks observed at the three other stations are: 57 and 26 min at Ensenada; 32, 21 and 17 min at Zihuatanejo; and 15 and 10 min in Huatulco. These peaks in the tsunami spectra are also prominent in the background spectra, indicating their topographic resonance nature.

4.3. Spectral Ratios (Source Functions)

Figure 13 presents the spectral ratios (source functions), $R_j(\omega)$, estimated from (6) for the six tsunami and background spectra shown in Fig. 12. They are not overly similar to the 2010 ratios (Fig. 8), apparently because the 2014 tsunami signal was much weaker and, consequently, the signal-to-noise ratio was much lower (the s/n ratio is a key factor determining the accuracy of $R_j(\omega)$ estimates). However, in general, the 2014 spectral ratios are internally consistent and, therefore, representative of the overall spectra for the event. As with 2010, the $R_j(\omega)$ for the 2014 tsunami do not have specific peaks associated with coastal topographic resonance (peaks that are clearly evident in the spectra shown in Fig. 12). Compared with the 2010 ratios, the 2014 ratios are approximately one order of magnitude smaller ($R_j(\omega) \sim 10^2$ versus 10^1, respectively; Figs. 8, 13) and occupy a narrower frequency band of $\sim$0.4–20 cph (periods, 2.5 h to 3 min). The maximum amplification of the tsunami waves relative to the background noise occurs at frequencies 2–4 cph (periods of 30–15 min).

Table 4

Parameters of the Chilean tsunami of 16 September 2015 recorded on the coast of Mexico (Main shock, M_w 8.3 at 22:55 UTC)

Station	Sampling (min)	First wave			Maximum waves			Observed tsunami variance (cm^2)	Visually estimated period (min)
		Arrival time (UTC)	Travel time (hh:mm)	Amplitude (cm) Sign	Amplitude (cm)	Time (UTC) of max amplitude	Wave height (cm)		
Ensenada	1	11:46	12:51	+17	17	11:58	34	33.6	25, 20
San Quintin	1	?	?	?	3	14:36	7	7.3	55
La Paz	1	10:30	11:35	+8	11	14:17	21	16.7	23
Mazatlan	1	9:36	10:41	+8	10	20:35	18	7.1	50, 6
Puerto Vallarta	1	9:46	10:51	+5	11	10:39	25	13.9	8
Manzanillo	1	8:37	09:42	+8	33	2:22[a]	64	94.8	30
Lazaro Cardenas	1	8:07	09:12	+5	12	21:38	26	14.5	60, 15
Acapulco	1	7:49[b]	08:54	+7	24	10:38	47	65.7	10
Puerto Angel	1	8:18	09:23	+6	40	10:47	75	69.6	5
Huatulco	1	7:17	08:22	+7	31	10:46	54	95.9	9
Salina Cruz	1	7:43	08:48	+22	23	0:51[a]	51	71.7	25, 17
Puerto Madero	1	7:27	08:32	+21	44	15:43	85	145.2	30
DART 43412	1[b]	8:04	09:09	+2.7	2.9	9:05	4.9	–	44, 7.5
DART 43413	1[b]	6:39	07:44	+2.2	2.3	8:18	4.4	–	28, 7.5

All times are in UTC for 17 September 2015, except where indicated

[a] 18 September 2015

[b] Event mode data

5. *The Chile (Illapel) Tsunami of 16 September 2015*

On 16 September 2015 a destructive (M_w 8.3[5]) interplate thrust-type earthquake occurred at 19:54:33 Local Chilean Time (22:54:33 UTC) in the region of Coquimbo, central Chile (Ye et al. 2016; Li and Ghosh 2016). According to the US Geological Survey (USGS), the epicenter of the earthquake (31.570°S; 71.670°W; 25 km depth) was located offshore, 48 km west of Illapel and approximately 480 km north from the epicenter of the 2010 earthquake (Fig. 1). This was the third great earthquake in the subduction zone along the coast of Chile in the last 5.5 years. The 2015 source region had been previously identified as a seismic gap, with prior large earthquakes in this region in 1730, 1880 and 1943 (Ye et al. 2016). The rupture covered the zone from approximately 28.5–32°S, for a length of around 400 km (Fig. 1).

The earthquake generated a major trans-oceanic tsunami (cf. Heidarzadeh et al. 2016; Tang et al. 2016; Omira et al. 2016) that was recorded by all tide gauges located along the coast of Chile; the maximum amplitude (zero-to-crest) of 4.6 m was measured at Coquimbo (Calisto et al. 2016; Contreras-López et al. 2016; Fuentes et al. 2016). Several post-tsunami field survey teams thoroughly explored the coast and found the following maximum run-up heights: 10.8 m at 30.365°S, 71.67°W (Aránguiz et al. 2016); 13.6 m at 30.97°S, 71.65°W (Contreras-López et al. 2016); and 11.4 m at 30.493°S, 71.690°W (Fuentes et al. 2016). Tsunami waves created severe damage in the near-field coastal zone, especially in the Coquimbo region located ~100 km north of the epicenter. At least 15 deaths were attributed to the tsunami. The unprecedented mass evacuation of over one million people from coastal areas organized by Chile's emergency service prevented a much higher death toll (Tang et al. 2016).

Aside from the Chilean coast, there was no other noticeable damage, despite the fact that the tsunami was recorded throughout the Pacific Ocean, including the coasts of Japan, New Zealand, Hawaii, Canada and the US and by a large number of DART stations located in the open ocean (Heidarzadeh et al. 2016; Tang et al. 2016). These waves were also measured

---

[5] M_w 8.4 according to Heidarzadeh *et al.* (2016).

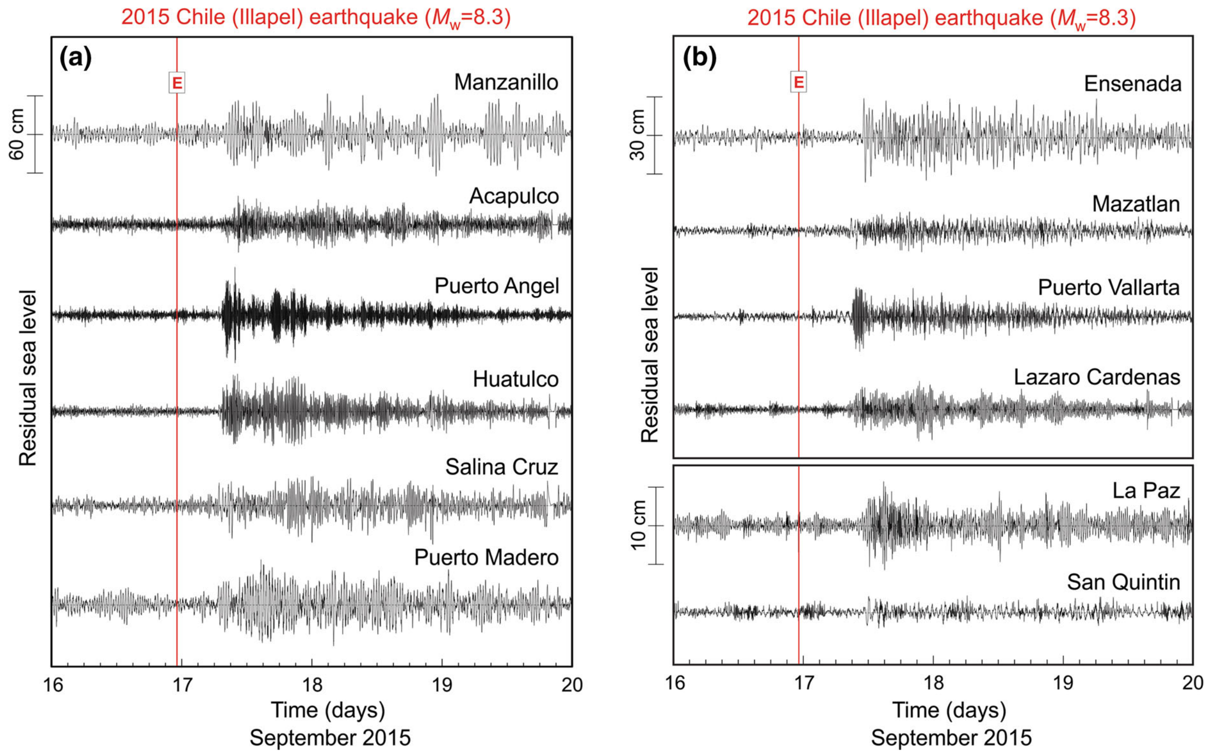

Figure 14
As in Fig. 4 but the for twelve coastal tide gauges that recorded the 16 September 2015 Chilean tsunami

by many coastal tide gauges in Mexico and by DART stations offshore of Mexico.

5.1. *Tsunami Observations*

The 2015 Chile (Illapel) tsunami was recorded by twelve tide gauges[6] on the coast of Mexico (Table 4; Fig. 14a, b). All instruments had sampling intervals $\Delta t = 1$ min. The twelve instruments spanned the entire Pacific coast of Mexico, from the southernmost station Puerto Madero to the northernmost station Ensenada (Fig. 15). This enabled us to thoroughly examine the propagation and evolution of the 2015 Illapel tsunami along this coast. The important features of the recorded 2015 tsunami waves are as follows (Table 4; Figs. 14a, b, 15):

1. Tsunami waves of the 2015 event were smaller than for the 2010 Maule tsunami but greater than for the 2014 Iquique tsunami. The highest trough-to-crest wave heights were observed at Puerto Madero (85 cm), Puerto Angel (75 cm) and Manzanillo (64 cm); the smallest wave heights were at San Quintin (7 cm), Puerto Vallarta (18 cm) and Mazatlan (21 cm). In general, the observed tsunami wave heights for the 2015 event were 2–2.5 times smaller than for the 2010 event.
2. The 2015 tsunami waves arrived first at 7:27 UTC (8 h 32 min after the earthquake) at Puerto Madero, at 8:37 UTC (9 h 42 min) at Manzanillo, at 10:30 UTC (11 h 45 min) at La Paz and lastly at 11:46 UTC (12 h 51 min) at Ensenada. The tsunami signal at San Quintin was too weak to identify the exact tsunami arrival time at this station. The tsunami travel times were approximately 30 min shorter than for the 2010 tsunami (Table 2) and 1 h longer than for the 2014 tsunami (Table 3), in good agreement with the locations of the respective source areas (Fig. 1).
3. The visually estimated dominant periods of the recorded waves were quite variable, ranging from

---

[6] In actuality, this tsunami was recorded by a few more tide gauges, in particular, Guerrero Negro, but the records were of poor quality.

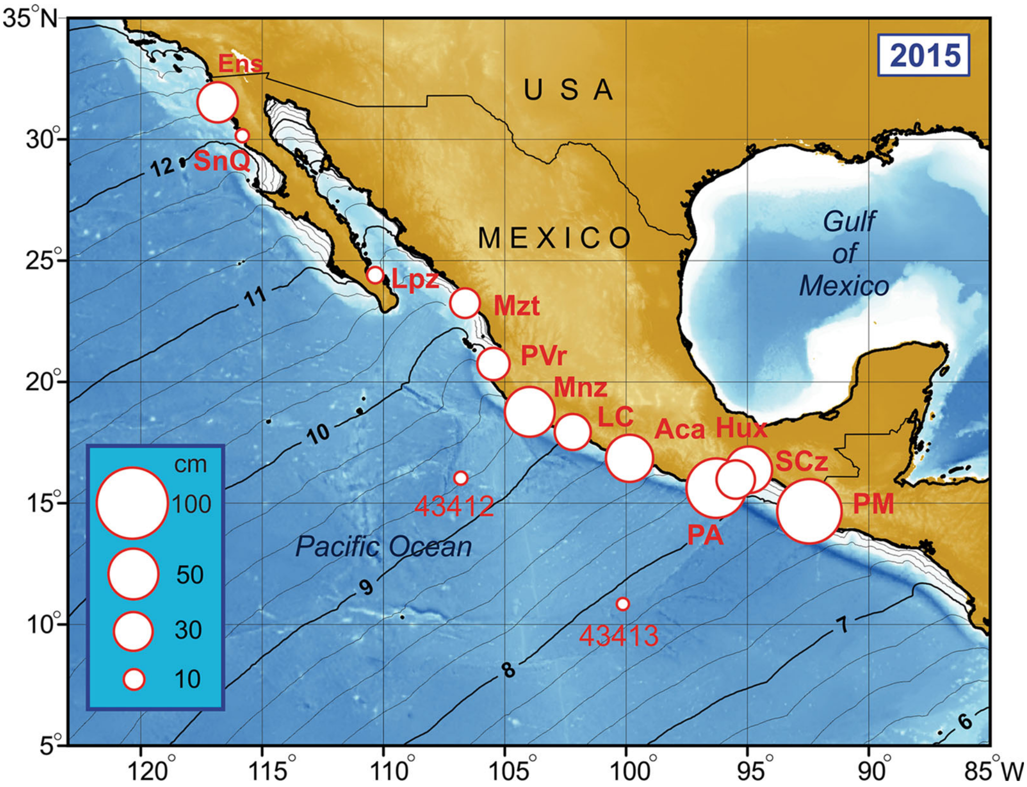

Figure 15

As in Fig. 5 but for the twelve coastal tide gauges and two DART stations that recorded the 2015 Chilean tsunami. The abbreviated names are: *Ens* Ensenada, *SnQ* San Quintin, *LPz* La Paz, *Mzt* Mazatlan, *PVr* Puerto Vallarta, *Man* Manzanillo, *LC* Lazaro Cardenas, *Aca* Acapulco, *PA* Puerto Angel, *Hua* Huatulco, *SC* Salina Cruz, and *PM* Puerto Madero. *Black solid lines* show the 2015 tsunami travel time (in hours and 15 min) from the source area computed using the wavefront orientation method (Fine and Thomson 2013)

5 min at Puerto Angel to 60 min at Lazaro Cardenas.

4. Maximum wave amplitudes at most sites were observed relatively soon (<2.5 h) after the first wave arrival. At Ensenada the first wave was the highest. However, there were a few exceptions: at Salina Cruz the maximum wave amplitude occurred 8 h after the first arrival, at Mazatlan and Puerto Madero 11–12.5 h and at Manzanillo and Salina Cruz about 1.5 days after the arrival of first tsunami wave.
5. Similar to the two other events, the tsunami ringing at all stations was quite long, lasting for more than three days (Fig. 9).

The mean tsunami wave height averaged over all twelve stations is 42.3 cm, which is 30 % higher than for the 2014 event and 2.3 times lower than for the 2010 event; the mean variance of the 2015 tsunami records is $Var_0 \sim 53$ cm^2, approximately 60 % larger than for the 2014 tsunami and five times smaller than for the 2010 tsunami. Based on statistical characteristics of the observed waves, we can separate all stations into two groups: “strong” (Puerto Madero, Puerto Angel, Manzanillo, Huatulco, Salina Cruz and Acapulco) and “weak” (Ensenada, Lazaro Cardenas, Puerto Vallarta, La Paz, Mazatlan and San Quintin). Maximum wave heights and variances for the first group are higher, while for the second group they were substantially smaller than the mean value. We note that all stations of the first group are located in the southern part of the region (Fig. 15).

Statistical characteristics of the coastal records have been compared with those from the open-ocean observations (Fig. 16). Unfortunately, DART 46412

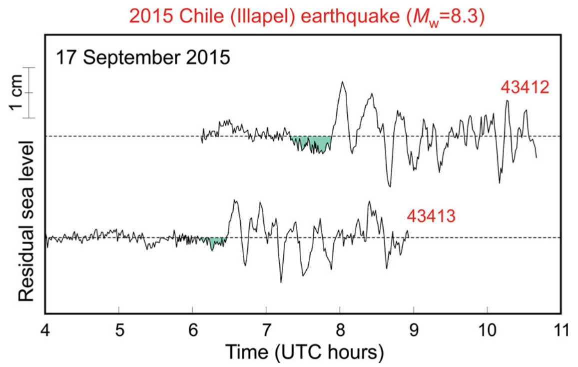

Figure 16
The same as in Fig. 6 but for DART records of the 16 September 2015 Chilean tsunami

located near Ensenada (Fig. 3) was not in operation during the 16 September 2015 event, while two other 'off-Mexico' DART stations (43412 and 43413) provide only 'Event-mode' data. The 'Event-mode' data were used to estimate the open-ocean tsunami parameters, which are found to be in good agreement with those obtained from the coastal measurements (Table 4). The arrival times at the DART stations match well with the arrival times at the coastal tide gauges and the theoretical ETA at the DARTs computed by the NTWC (Palmer, AK). More specifically, the NTWC arrival times of 06:35 (43413) and 08:00 (43412) are only 4 min shorter than the observed arrival times (Table 4). Tsunami travel times estimated from coastal and open-ocean measurements are in good agreement with the numerically computed travel times presented in Fig. 15.

The maximum observed open-ocean wave heights were approximately three times higher than for the 2014 tsunami (Table 3) and 2–3 times lower than for the 2010 tsunami (Table 2). This means that the tsunami height ratios, 2015/2010, for the open-ocean and coastal records were approximately the same, in contrast with the 2014/2010 and 2014/2015 ratios which were much smaller for the open-ocean than for the coastal wave heights.

The open-ocean records of the 2015 tsunami at DART sites 43412 and 43413 are characterized by a prominent leading positive wave with an amplitude of 2.2–2.7 cm. As with the 2010 and 2014 DART records, this leading wave was preceded by a small but detectable trough of 2.0–3.5 mm (Fig. 16). Similarly, a negative trough wave that outran the major positive frontal wave is also identified in coastal records having a relatively high *s*/*n* ratio (in particular, at Puerto Madero, Huatulco and Port Angel; see Fig. 14).

5.2. *Spectral Analysis*

Spectral analyses of the twelve 2015 tide gauge records (Table 4; Fig. 14a, b) followed the same procedure and examined the same parameters as for the 2010 and 2014 events. The properties of the tsunami and background spectra (Fig. 17a, b) are comparable to those for the 2010 (Fig. 7) and 2014 (Fig. 12) tsunamis. Three tide gauges are common to all three events: Manzanillo, Lazaro Cardenas and Acapulco. The 2015 major spectral peaks observed at these stations were: 30, 10 and 7.5 min at Manzanillo, 30 min at Acapulco, and 58 and 15 min at Lazaro Cardenas, which are approximately the same periods observed during the 2010 and 2014 events. Similarly, the 2015 spectral peaks at Ensenada (47, 28 and 18 min) and Huatulco (30, 15 and 10 min) closely match the periods of the major 2014 spectral peaks at these stations.

In general, the coastal spectra are strongly variable from one station to another and characterized by marked spectral peaks. Most of these peaks for the tsunami and background spectra have similar periods. These spectral peaks, which are different at each station, are indicative of the strong influence of bathymetric and topographic effects on coastal sea level oscillations. The coincidence of tsunami and background spectral peaks implies that the periodicity of the recorded tsunami waves is mainly related to the resonant properties of the local/regional bathymetry and basin dimensions rather than to the frequency characteristics of the incoming waves. It is for this reason that the spectra of tsunamis from the three Chilean earthquakes are so similar at the same locations. Bathymetry and coastal topography play a much more important role in determining the spectral properties of tsunami waves at individual sites than the source parameters.

The most prominent spectral peaks observed at other stations, other than those mentioned above are:

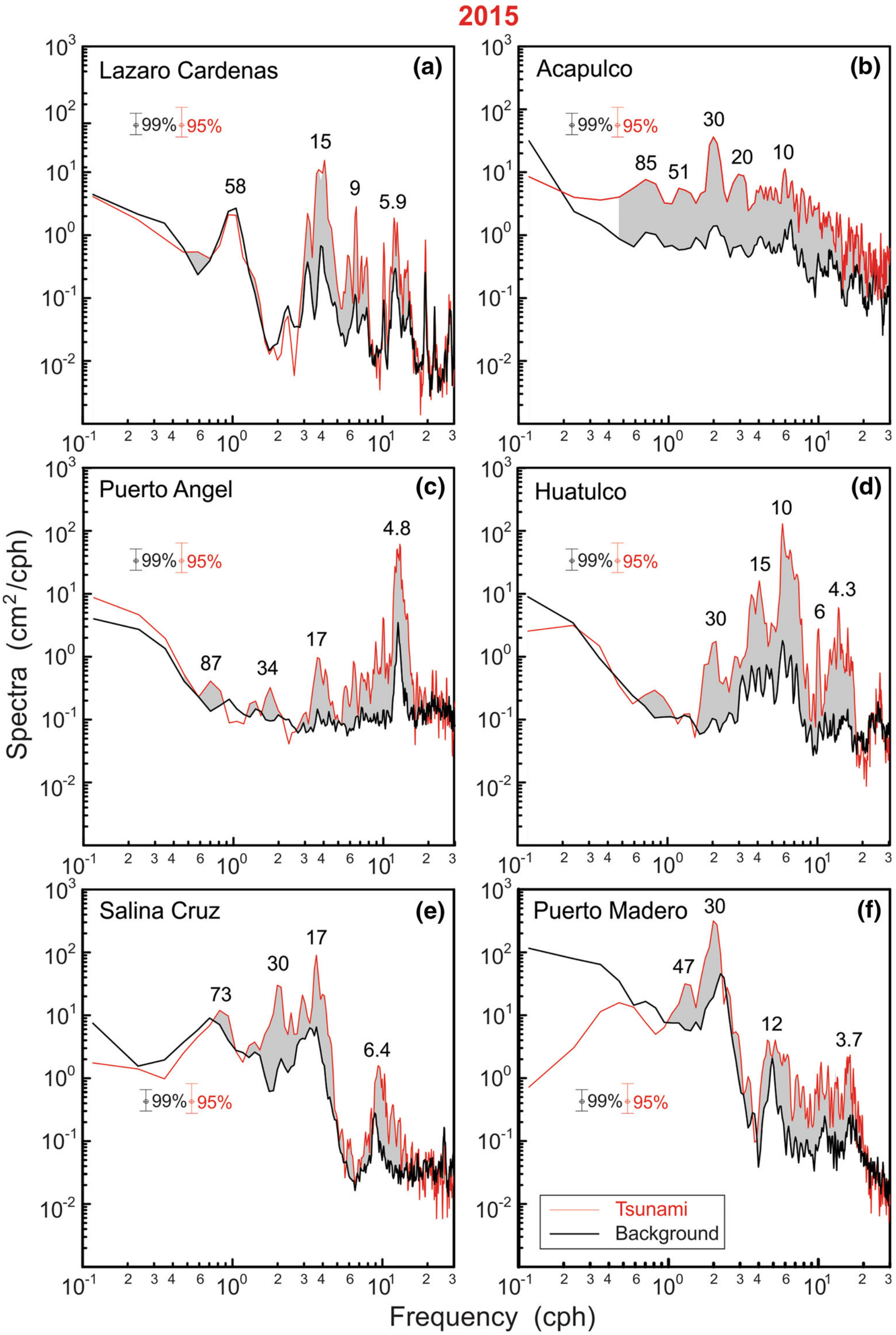

Figure 17
As in Fig. 7 but for the 2015 spectra

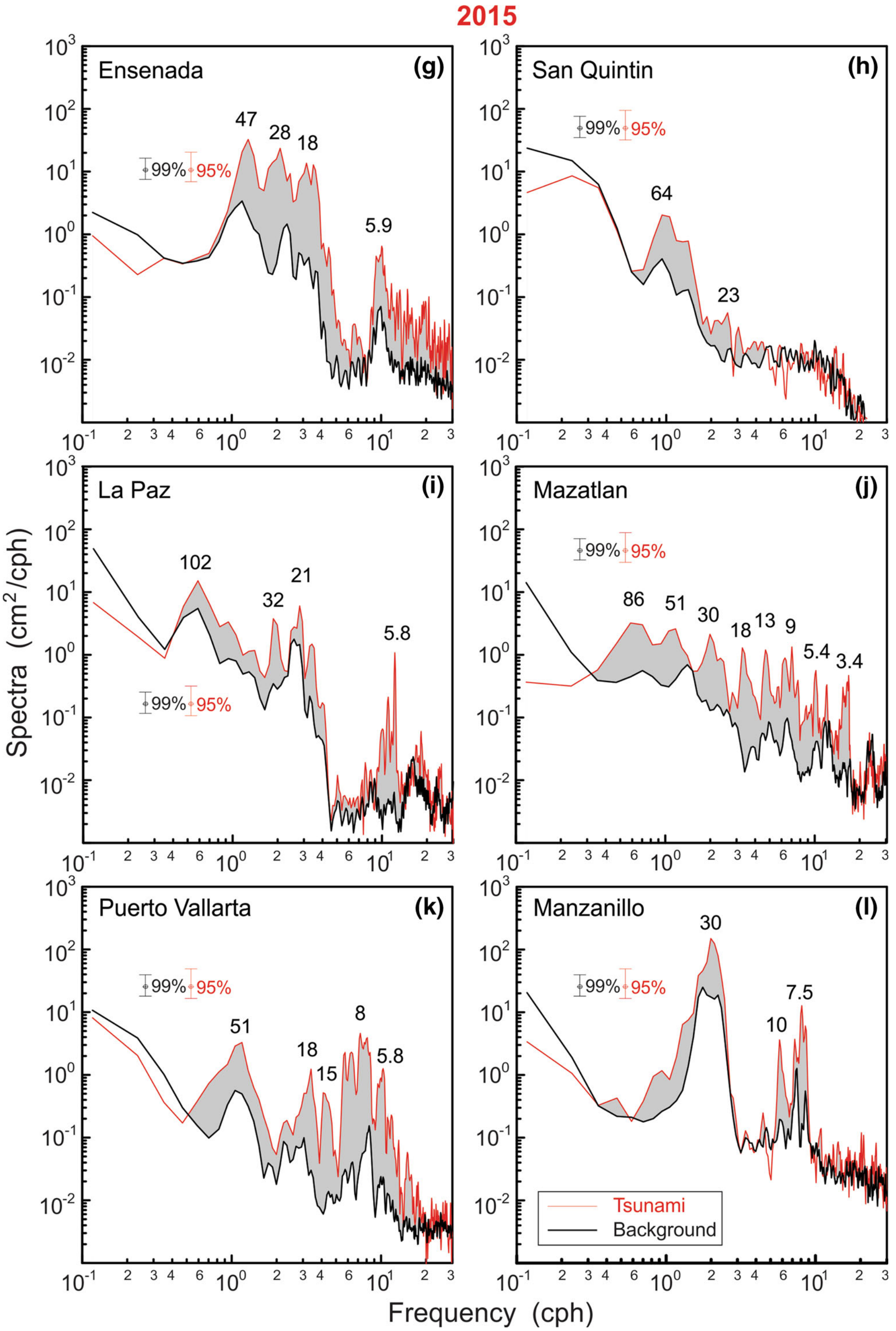

Figure 17
continued

- A peak of 4.8 min at Puerto Angel; this peak coincides with a sharp and narrow peak in the background spectrum and accounts for the strong monochromatic high-frequency oscillations observed at this station.
- Peaks of 30, 17 and 6.4 min at Salina Cruz that also match the respective background peaks.
- A major long-period peak of 102 min at La Paz, apparently associated with the fundamental mode of La Paz Bay, and three other prominent peaks of 32, 21 and 5.8 min likely associated with local eigen modes.
- Highly complicated spectral structure at Mazatlan and Puerto Vallarta, with numerous spectral peaks of comparable magnitude.
- Highly amorphous tsunami and background spectral distributions at San Quintin, indicating that arriving waves with periods less than 40 min are strongly suppressed by a local topographic response[7]; this may explain why observed tsunami waves at this station are weaker than at any other station.

5.3. *Spectral Ratios (Source Functions)*

Tsunami and background spectra are shown in Fig. 17a, b have been used to estimate the spectral ratios (source functions), $R_j(\omega)$, for the twelve stations along the coast of Mexico (Fig. 18a, b) based on expression (6). The estimated ratios are in reasonable agreement with each other (except San Quintin, which is significantly different), and therefore, represent the general spectral properties of the source. Similar to the 2010 and 2014 ratios, the 2015 $R_j(\omega)$ functions do not have particular resonant peaks associated with local bathymetry and basin dimensions, which is evident in the respective tsunami spectra (Fig. 17a, b). The 2015 ratios are approximately of the same order of magnitude as those for the 2014 tsunami (Fig. 13) and about one order lower than the 2010 ratios (Fig. 8). Significant tsunami spectral ratios ($R_j(\omega) > 1.0$) occupy a frequency band of $\sim$0.4–30 cph (periods from 2.5 h to 2 min). The maximum amplification of the tsunami waves relative to the background noise occurs at frequencies 2–20 cph (periods 30–3 min).

6. *Open-Ocean Tsunami Spectra*

As indicated previously, the local/regional seafloor topography strongly determines the characteristics of coastal tsunami records. The tsunami wave spectra in Figs. 7, 12 and 17a, b mainly mimic the individual resonant features of specific sites rather than the particular spectral characteristics of the source regions of the 2010, 2014 and 2015 tsunamis. The approach proposed by Rabinovich (1997) makes it possible to reconstruct the open-ocean tsunami spectra by suppressing the bathymetric influence. The three events recorded on the Mexican coast provide an exceptional opportunity to compare the deep-sea tsunami spectra "reconstructed" from the coastal sites with the deep-sea tsunami spectra estimated directly from open-ocean DART measurements. The Mexican tsunami records enable us to verify the Rabinovich (1997) approach and to obtain reliable estimates of the offshore spectral properties of the three tsunamis. The records also enable us to compare the three events and their seismic source parameters.

According to (2), the observed open-ocean long-wave spectrum, $E_{\mathrm{obs}}(\omega)$, during the tsunami event may be represented as

$$E_{\mathrm{obs}}(\omega) = E_{\mathrm{tsu}}(\omega) + E_0(\omega). \tag{7}$$

Thus, if the background spectrum, $E_0(\omega)$, is known (for example, from the observations at the specific site before the event), then the "true"(unaltered) tsunami spectrum, $E_{\mathrm{tsu}}(\omega)$, can be estimated as the difference between the observed and background spectra. The DART deep-ocean sea level observations enable us to obtain direct estimates of the open-ocean tsunami spectra. At the same time, the open-ocean tsunami spectra can be evaluated from the coastal observations. Using (4a, 4b) and (6), we can express these spectra in the form:

---

[7] A very similar situation is observed at Prince Rupert on the northern coast of British Columbia where only ultra-long tsunami oscillations are recorded (with $T > 1$ h), while high-frequency signals arriving at this station are strongly attenuated (filtered) by Dixon Entrance (a wide strait) and by the shelf adjacent to the station, playing the role of an effective low-pass filter (Rabinovich et al. 2013a).

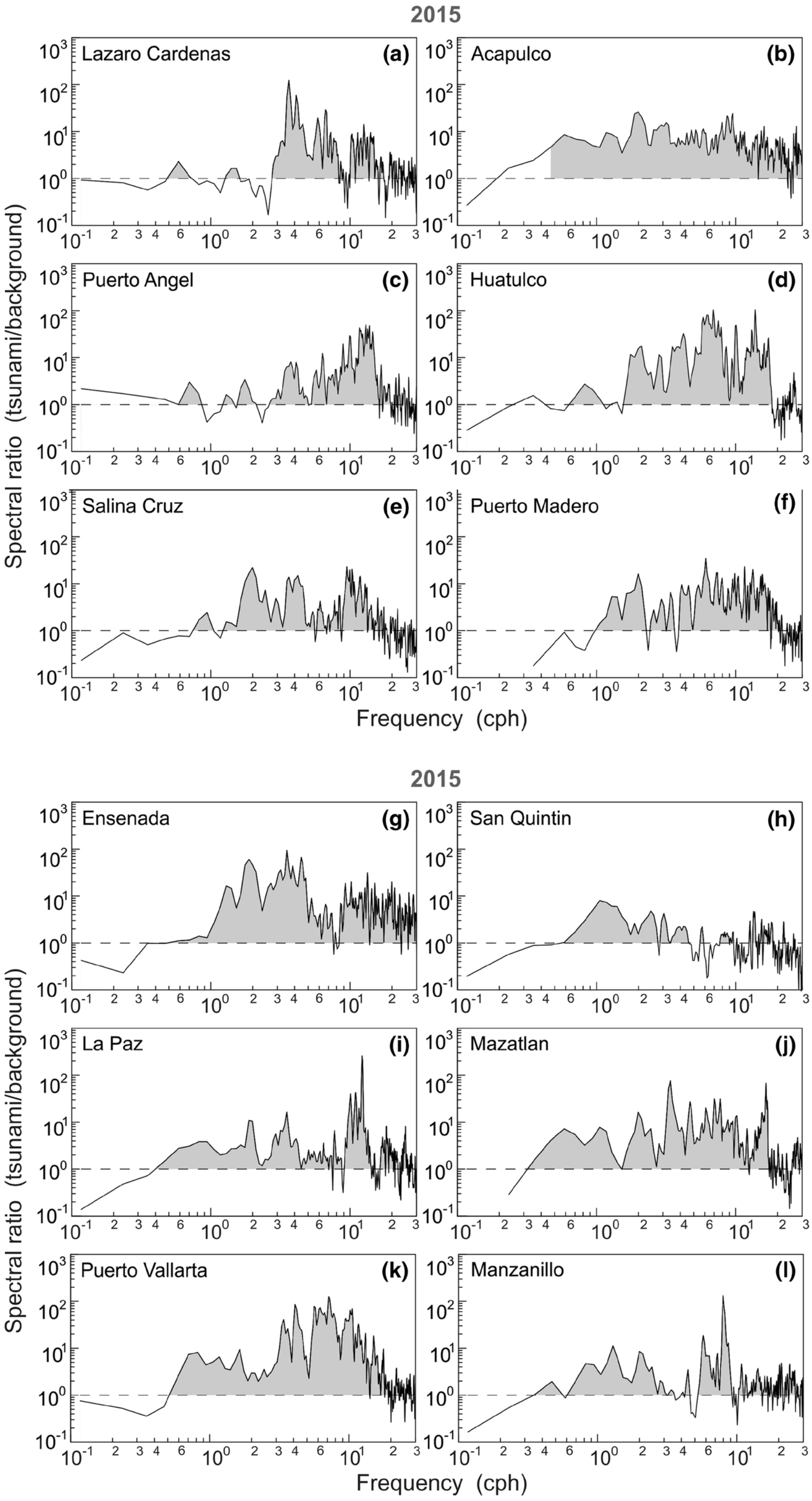

Figure 18
As in Fig. 8 but for the twelve 2015 spectra shown in Fig. 17

$$E^j_{\mathrm{obs}}(\omega) = \left[E^j_{\mathrm{tsu}}(\omega) + E_0(\omega)\right] = R_j(\omega)E_0(\omega); \quad (8a)$$

$$E^j_{\mathrm{tsu}} = \left[R_j(\omega) - 1.0\right] E_0(\omega), \quad (8b)$$

where $R_j(\omega)$ is the spectral ratio estimated for a specific coastal site. Thus, if $E_0(\omega)$ is known from the offshore measurements, we can use (8a) and (8b) to reconstruct "individual" open-ocean spectral characteristics of tsunami waves, $E^j_{\mathrm{obs}}(\omega)$ and $E^j_{\mathrm{tsu}}(\omega)$, based on coastal measurements. However, reasonable approximation of these characteristics can also be obtained without exact knowledge of the offshore background spectrum in the vicinity of specific site. Numerous deep-sea long-wave observations in the Pacific Ocean (cf. Kulikov et al. 1983; Filloux et al. 1991; Rabinovich 1997) indicate that the background spectrum in the open ocean, $E_0(\omega)$, in the tsunami frequency band is nearly spatially uniform, highly steady over time, and has the form:

$$E_0(\omega) \ = \ A_0\omega^{-2.0}. \quad (9)$$

The expressions (8a, 8b) and (9) enable us to approximate tsunami spectra in the open ocean based on observations at particular coastal tide gauges.

There is, however, a problem. The spectral ratio, $R_j(\omega)$, is a *random function* that strongly depends on the characteristics of the local background noise, in particular on the consistency of the noise spectrum *before* and *during* the event. This, in turn, depends on the concurrent atmospheric processes, which are the main forces driving the local oscillations. It is because of this force the spectral ratio $R_j(\omega)$ at different sites are similar, but not identical, for each event (Figs. 8, 13, 18a, b).

To improve the reliability of the source function estimates and to increase the number of degrees of freedom, we can average $R_j(\omega)$ for certain groups of N stations, viz,

$$\hat{R}(\omega) = \frac{1}{N}\sum_{j}^{N} R_j(\omega), \quad (10)$$

where $\hat{R}(\omega)$ is the "*mean spectral ratio*". We assume that averaging allows us to suppress individual random outliers of $R_j(\omega)$ so as to reveal the underlying properties of these functions and, consequently, estimate the "general" spectral characteristics of tsunami waves, $E_{\mathrm{obs}}(\omega)$ and $E_{\mathrm{tsu}}(\omega)$. We have used this approach, here, to define the open-ocean spectral characteristics of the 2010, 2014 and 2015 tsunamis.

The steps used in our new method for reconstructing open-ocean tsunami spectra based on coastal tide gauge measurements are summarized below:

1. Estimate the individual tsunami spectra, $S^j_{\mathrm{obs}}(\omega)$, from coastal records (the lengths of the records should be between 8 h and 1.5 days).
2. Estimate the background spectra, $S^j_{\mathrm{bg}}(\omega)$, from the respective coastal records; these records should of sufficient length (more than several days) to increase the number of degrees of freedom in the dominator of estimated spectral ratios and be obtained immediately before the tsunami arrival.
3. Estimate the individual spectral ratios tsunami/background for the coastal stations, $R_j(\omega) = S^j_{\mathrm{obs}}(\omega)/S^j_{\mathrm{bg}}(\omega)$, and average them over a group of stations to estimate the "mean spectral ratio", $\hat{R}(\omega)$.
4. Reconstruct the open-ocean tsunami spectrum, $E_{\mathrm{tsu}}(\omega) = \hat{R}(\omega)\ E_0(\omega)$, where $E_0(\omega)$ is the open ocean background taken from observations or roughly approximated as proportional to $\omega^{-2.0}$.

6.1. 2010

To estimate directly the open-ocean tsunami and background spectra from DART stations, we need sufficiently long high-quality and high temporal resolution data that can only be obtained from the retrieved instruments. For the 2010 event, there were two such instruments (DARTs 46412 and 43413) working in the region offshore from Mexico (Fig. 2). The spectral analysis procedure for the DARTs was the same as for the coastal data. To estimate background spectra, we applied 6-day pre-tsunami records (33,792 values of 15 s data), while for the tsunami spectra, we used 34 h segments (8192 values). The length of the KB-window was chosen to be 512 min, yielding $\nu = 64$ degrees of freedom for the background spectra and $\nu = 14$ for the tsunami spectra. The spectral resolution for all spectra was $\Delta f \approx 0.117$ cph and the Nyquist frequency $f_n = 120$ cph. The computed tsunami and background spectra for DARTs 46412 and 43413 are shown in Fig. 19a. Using (7), we also estimated the

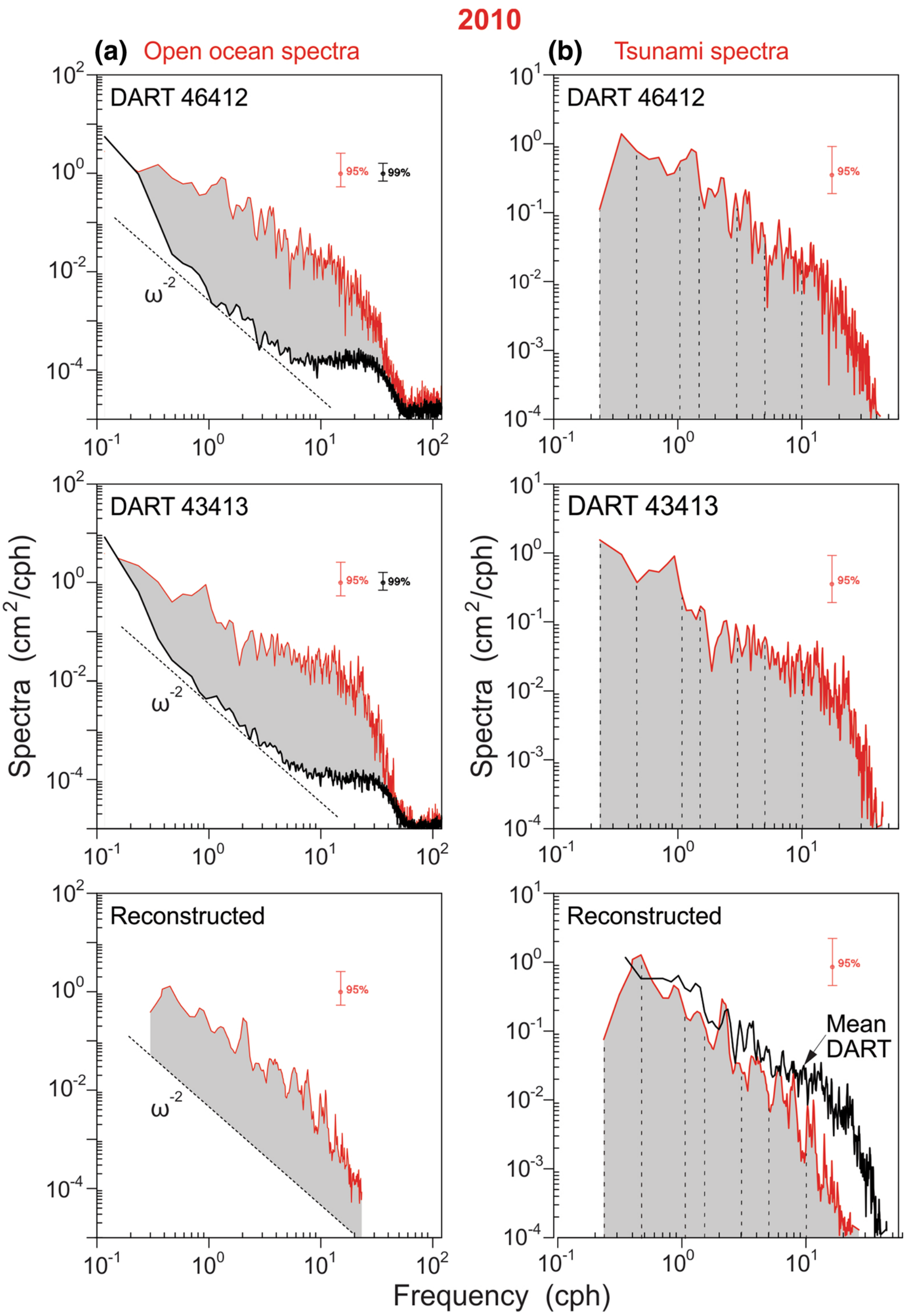

Figure 19

Open-ocean sea level spectra derived for the 2010 Chilean tsunami offshore of Mexico. **a** Spectra of the background (pre-tsunami) and tsunami oscillations for DART 46412 (*upper panel*) and 43413 (*middle panel*). The 95 % confidence level applies to the tsunami spectra, the 99 % confidence level to the background spectra. The tsunami spectrum reconstructed from the coastal observations is shown in the *bottom panel*. A frequency-dependent reference spectral power law, $E \sim \omega^{-2}$, is denoted by the *thin solid straight line*. **b** “True” (bathymetrically unaltered) tsunami spectra obtained by subtracting the background spectra from the observed spectra. *Vertical dashed lines* divide the tsunami frequency band into seven partitions

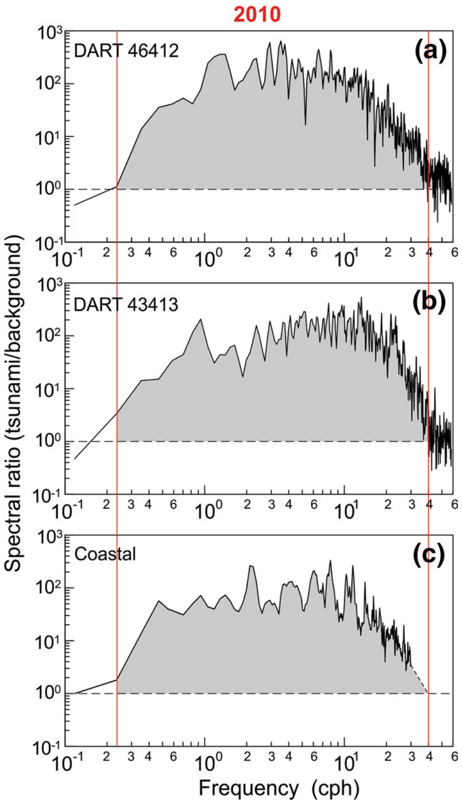

Figure 20
Tsunami/background spectral ratios for **a** DART 46412; **b** DART 43413 and **c** the "mean spectral ratio", $\hat{R}(\omega)$, estimated from coastal observations. *Shaded areas* denote the response associated with the arriving tsunami waves (i.e., the amplification of the spectra due to the tsunami measured relative to the background spectra). The *solid vertical red lines* border the tsunami frequency band

"true" tsunami spectra, $E_{\text{tsu}}(\omega)$ (Fig. 19b). The "observed" tsunami and background spectra were used to calculate the open-ocean spectral ratios, $R(\omega)$; the ratios for DARTs 46412 and 43413 are presented in Fig. 20a, b, respectively.

We also computed the "coastal" spectral ratios, $R_j(\omega)$, and averaged them according to (10) to estimate the "mean spectral ratio" $\hat{R}(\omega)$ (Fig. 20c). We were encouraged to find that the three totally independent ratios shown in Fig. 20 (two open-ocean ratios evaluated directly from the DART spectra and the mean coastal ratio) are highly similar. Specifically, the spectral ratios for those values of $R_j(\omega) > 1.0$, shown as the shaded areas associated with the tsunami, occupy the same frequency band of $\sim$0.25–40 cph (periods from 4 h to 1.5 min), have almost identical "dome-like" shapes and have comparable absolute values. Such good agreement demonstrates the reliability of the proposed approach and enables us to make conclusions regarding the spectral properties of the original source area. The results further enable us to reconstruct the open-ocean tsunami spectrum based on coastal measurements alone (Fig. 19, bottom layer).

In general, the "dome-like" shapes of the tsunami/background spectral ratios (source functions) for the 2010 event, reconstructed from the Mexican coastal tide gauges (Fig. 8), are consistent with the corresponding functions estimated from for coastal tsunami records for the coasts of British Columbia (Rabinovich et al. 2013a) and the Kuril Islands (Shevchenko et al. 2013), and from offshore deep-ocean DART records throughout the Pacific Ocean (Rabinovich et al. 2013b). For all of these regions, the tsunami energy spans roughly the same frequency band from 0.2–0.25 to 30–40 cph (periods from 5–4 h to 2–1.5 min) that appears to be dictated by the seismic source regions (Fig. 1).

The "true" tsunami spectra (Fig. 19b) have a specific shape of a right triangle with most of the energy concentrated at low frequencies and a gradual energy decay with increasing frequency. The relatively sharp boundary of the low-frequency energy distribution is likely associated with the maximum source length and, consequently, with maximum tsunami wave period that can be generated by this particular source.

6.2. 2014

The previous analyses were repeated for the 2014 event. Unfortunately, there were no continuous 15-s data available for the DART stations (46412, 43412 and 43413) located in the Mexican offshore region, so that we were required to use data from three other DART sites (46411, 51406 and 51407; Fig. 2b) located farther away but still relatively close to the region under study. We also used the spectra and spectral ratios from six coastal tide gauges (Figs. 12, 13). The open-ocean spectra from the three DARTs and the average spectrum reconstructed from the coastal spectra are shown in Fig. 21; the corresponding spectral ratios are presented in Fig. 22.

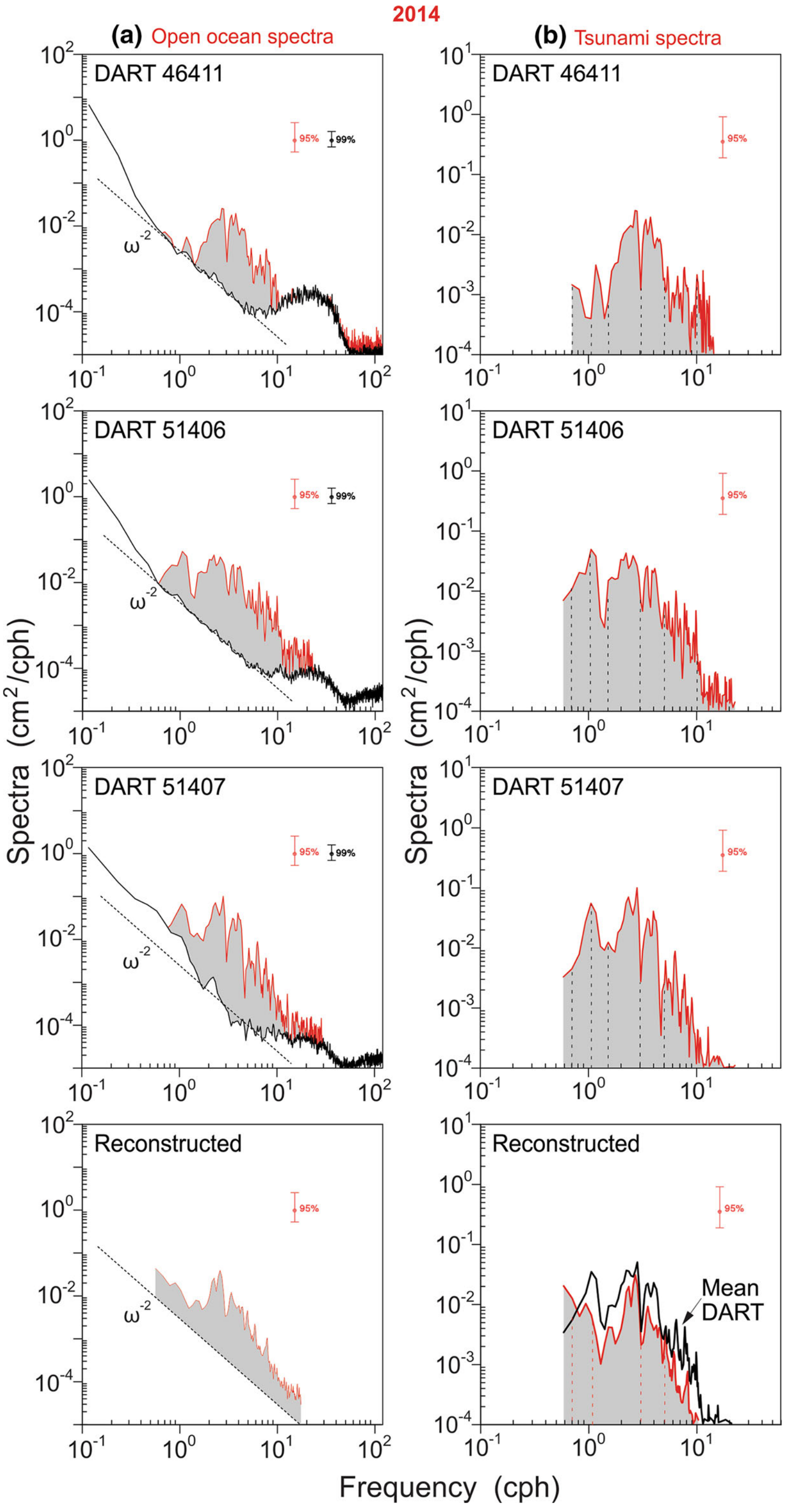

Figure 21
As in Fig. 19 but for the 2014 tsunami. The open-ocean spectra for DARTs 46411, 51406 and 51407 (see Fig. 2b for DART locations) are shown in the *three upper panels*; the tsunami spectrum reconstructed from the coastal observations is shown in the *bottom panel*

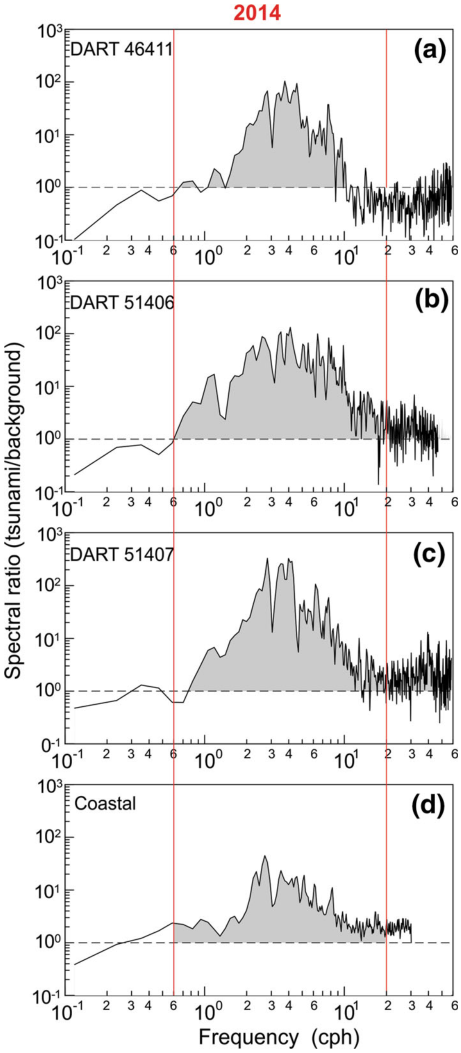

Figure 22
As in Fig. 20 but for the 2014 Chile tsunami and spectra shown in Fig. 21

The spectra and spectral ratios estimated from direct DART open-ocean measurements and those based on coastal observations are in reasonable agreement. In particular, the mean spectral ratio calculated from the six coastal ratios (Fig. 22d) spans the same frequency band and has the same general shape as the three open-ocean spectral ratios (Fig. 22a–c). The main difference is in the absolute values: $\hat{R}(\omega)$ estimated from the coastal data is noticeably smaller than $R(\omega)$ estimated for the three DART stations. Consequently, the open-ocean tsunami spectrum reconstructed from coastal data (Fig. 21, bottom panels) has lower spectral values than those from deep-ocean records for the same frequencies (Fig. 21, three upper panels). This is because, for the 2014 event, the pre-tsunami background noise relative to the tsunami signal was much greater at the coastal stations than at the open-ocean stations.

One of the most noteworthy findings is the marked difference in the 2014 tsunami spectra and spectral ratios compared to those for the 2010 tsunami (compare Figs. 21 and 22 with Figs. 19 and 20). For the 2014 event, the recorded tsunami waves occupied the frequency band from 0.7 to 20 cph (periods from ~1.5 h to 3 min), while the peak $R(\omega)$ values were in the band 2–6 cph (periods of 30–10 min) and the maximum "true" tsunami spectral energy, $E_{\mathrm{tsu}}(\omega)$, was in the 1–4 cph (60–15 min) band. This means that the 2014 tsunami was much more "high-frequency" relative to the 2010 tsunami, apparently because of the much smaller lateral extension of the source area (Fig. 1).

6.3. *2015*

Only a few DART stations in the Pacific Ocean were retrieved after the 16 September 2015 Chile tsunami. As a consequence, there were very few continuous 15-s open-ocean data available for spectral analysis of this event. Only one DART site (46411), located relatively close to the coast of Mexico (Fig. 2c), had these data. In contrast, we had access to 12 adequate tide gauge records for Mexican coast for this event (Fig. 15). Excluding San Quintin (which had unreasonable spectra: see Figs. 17h, 18h), this large number of coastal records enabled us to separate them into two groups: "southern" (Figs. 17a–f, 18a–f) and "northern" (Figs. 17g, i–l, 18g, i–l) and to evaluate for each group independent values of the "mean spectral ratio" and "reconstructed spectra". The results of the coastal record analyses are compared with the direct estimates of these characteristics from DART 46411 (Figs. 23, 24). Results resemble those for the 2014 event: the open-ocean DART 46411 spectra (Fig. 23 upper) and spectral ratio (Fig. 24a) correspond well to the reconstructed spectra (Fig. 23 middle and bottom) and mean spectral ratios (Fig. 24b, c) calculated for coastal stations. Once again, we are encouraged by the good agreement in the results obtained from two

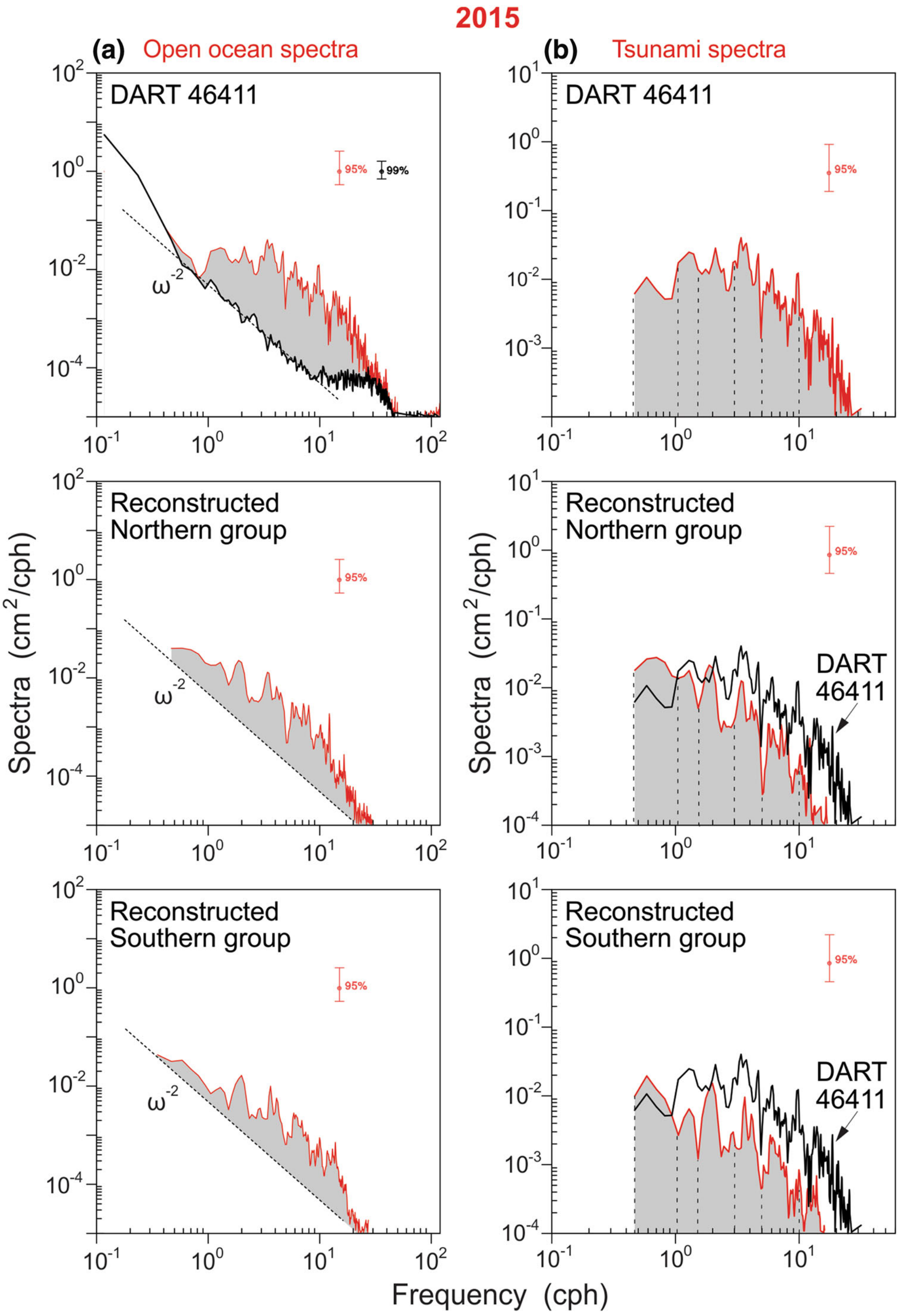

Figure 23

a Open-ocean sea level spectra of the background (pre-tsunami) and the 2015 Chilean tsunami offshore of California recorded at DART 46411 (*upper panel*) and the tsunami spectra reconstructed from the coastal spectra at the southern (*middle panel*) and northern (*bottom panel*) groups of stations (the respective spectra are shown in Fig. 17). The 95 % confidence level applies to the tsunami spectra, the 99 % confidence level to the background spectra. A reference frequency-dependent spectral power law, $E \sim \omega^{-2}$, is denoted by the *thin solid straight line*. **b** Respective "true" (bathymetrically unaltered) tsunami spectra estimated by subtraction of the background spectra from the observed (reconstructed) spectra. *Vertical dashed lines* divide the entire tsunami frequency band into seven partitions

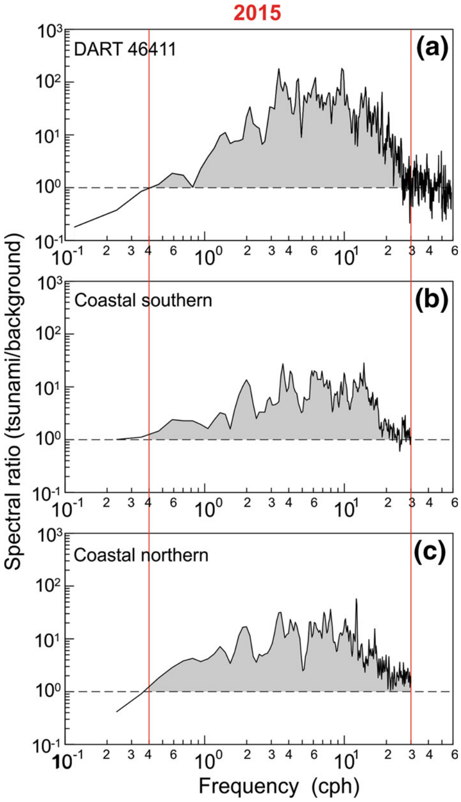

Figure 24

Tsunami/background spectral ratios for **a** DART 46411; and the "mean spectral ratios" $\hat{R}(\omega)$ estimated using the coastal observations for the **b** southern and **c** northern groups of stations. *Shaded areas* denote the tsunami response of the arriving waves (i.e., the amplification of the spectra arising from the tsunami waves and measured relative to the background spectra). The *solid vertical red lines* border the tsunami frequency band

totally independent groups of stations. Specifically, the tsunami frequency band, the general shape and even the magnitude of $\hat{R}(\omega)$ for the northern and southern groups of stations are alike. All of these features, except for the absolute values of $\hat{R}(\omega)$, are quite similar to those that were directly evaluated from DART 46411.

The "true" 2015 tsunami spectra have a shape that lies between the shapes of the 2010 and 2014 spectra. The "reconstructed spectra' (from the two groups of coastal observations) are only slightly lower than the actual 46411 tsunami spectrum. The tsunami frequency band of 0.4–30 cph (periods, 2.5 h–2 min), as indicated in Fig. 24 by the red vertical lines, is especially well defined. The frequency range is a little wider than for the 2014 tsunami but narrower than for the 2010 tsunami, consistent with the relative spatial extent of the 2015 source area compared to that for the two other events (Fig. 1).

7. Discussion

One of the key requirements for modern tsunami research is to define specific fundamental parameters of tsunami waves that adequately describe the event and can be used for effective tsunami warning (Tang et al. 2012; Titov et al. 2016). Several attempts have been made to define tsunami wave scales that would allow comparisons between different events. Two parameters that are presently used for this purpose are '*tsunami intensity*', which is based on estimates of the average wave heights along the nearest coast, and '*tsunami magnitude*', which is evaluated from tide gauge measurements of the maximum observed tsunami wave height within a specified distance of the epicenter (http://ngdc.noaa.gov/hazard/tsu_db.shtml). The main shortcoming of both parameters is that they are exclusively based on coastal records, whereby they are more indicative of the resonant topographic properties of particular sites, or even individual instruments, rather than the characteristics of the tsunami source itself.

The shortcoming noted above is probably the main reason why seismic parameters, in particular, the momentum magnitude, M_w, are still widely used to characterize the major properties of the tsunami source and the destructive potential of the generated waves (Titov et al. 2016). However, traditional seismic analysis is inadequate to accurately predict the tsunami energy. For example, the Sumatra earthquake of 28 March 2005 (M_w 8.6) did not generate a major tsunami as had been expected from the earthquake magnitude (Tang et al. 2012). Tsunami prediction and warnings based solely on seismic parameters produce a large number of false alarms (cf. Titov 2009). It is evident that the tsunami source energy would be the most informative and important parameter to characterize tsunami events.

The numerous offshore DART stations deployed in past years along the Fire Rim of the Pacific Ocean enable us to evaluate tsunami parameters, including the source energy and open-ocean tsunami energy, that have been unaffected by local topographic and bathymetric effects. Tang et al. (2012) and Titov et al. (2016) recently proposed a real-time approach to determine tsunami source energy through the inversion of DART data being collected during the time of tsunami propagation. They indicated that the total tsunami energy is the critical source parameter; smaller-scale details, including the exact ratio of kinetic to potential energy, are of second order importance for far-field tsunami propagation. According to the DART-based estimates of Titov et al. (2016), the tsunami source energy of the 2010 Chile tsunami was $E_T = 1.6 \times 10^{15}$ J; for comparison, the corresponding estimates for the 2009 Samoa and 2011 Tohoku tsunamis were 1.2×10^{14} J and 3.0×10^{15} J, respectively.

The latter are *real-time* estimates of the source energy based on short ($\sim$1-h), DART measurements of tsunami wave arrival times in the near-source region. The purpose of the present analysis is (1) to obtain a posteriori estimates of open-ocean tsunami wave energy (i.e., tsunami *variance*) based on spectral analysis of far-field DART and coastal records, and (2) to compare spectral properties of these records. The "true" tsunami spectra for the three Chilean tsunamis are shown in Figs. 19b, 21b and 23b. To construct these spectra, we used 1.5-day tsunami records, corresponding to the *integral (mean) spectral properties* of the tsunami waves. Analysis of the open-ocean records of three major Pacific tsunamis (2009 Samoa, 2010 Chile and 2011 Tohoku) indicate that trans-oceanic energy diffusion, multiple reflection and scattering of tsunami waves lead to a smoothing of far-field integral spectral estimates and that 1.5 days is sufficiently long for these estimates to become stabilized and consistent (Rabinovich et al. 2013b).

Based on our spectral analyses (Figs. 19, 21, 23), we can integrate the energy in the tsunami frequency band, $\omega_{\text{begin}} < \omega < \omega_{\text{end}}$, and estimate the *integral tsunami energy,*

$$I_0 = \int_{\omega_{\text{begin}}}^{\omega_{\text{end}}} E_{\text{tsu}}(\omega) d\omega. \tag{11}$$

In Figs. 20, 22 and 24, the tsunami frequency bands for the different events are bordered by red vertical lines. The parameter I_0 evaluated for open-ocean tsunami DART measurements is independent of the influence of local bathymetric effects and is, therefore, a fundamental property of open-ocean tsunami waves. Moreover, the approach we have introduced in the present study demonstrates that the same characteristic can also be obtained from *coastal tide gauge measurements* by excluding the influence of local bathymetry and basin dimensions (as shown by Rabinovich 1997).

Figure 25 shows the parameter I_0 reconstructed from DART and coastal measurements for the three Chilean tsunamis. The scalar values of I_0 are denoted by the size of the respective circles. I_0 values calculated from coastal spectra closely resembles those derived from the open-ocean spectra. The mean values of I_0, denoted as $\hat{I}_0$, for the open ocean data from the three Chilean tsunamis are: 1.35 cm^2 (2010), 0.08 cm^2 (2014) and 0.09 cm^2 (2015). The mean open-ocean variance estimates represented by $\hat{I}_0$ can be compared with the mean variance of tsunami waves on the coast, $Var_0 = 278$ cm^2 (2010), 33 cm^2 (2014) and 53 cm^2 (2015). The square root of each variance ratio,

$$A = \sqrt{Var_0/\hat{I}_0}, \tag{12}$$

characterizes the relative amplification of tsunami waves as they arrive at the coast. For the three Chilean tsunamis, we derive the following values of A: 14.3 (2010), 20.3 (2014) and 24.3 (2015). Considering all the factors that have gone into these estimates, the values are remarkably similar, $\hat{A} \sim 20$, suggesting as a "rule-of-thumb" that an incoming tsunami wave with an open-ocean wave amplitude of 5 cm (as recorded by DART sites off the coast of Mexico) will produce 1 m tsunami wave amplitudes at tide gauge sites along the Mexican coast.[8]

In addition to the absolute values of I_0, as represented by the *size* of the circles in Fig. 25, we also estimated their *colour*, a measure of the open-ocean frequency content of each tsunami. The entire tsunami frequency band, $\omega_{\text{begin}} < \omega < \omega_{\text{end}}$, was separated into seven partitions (marked in Figs. 19b, 21b, 23b) and for each of these partitions we estimated the respective energy contribution (band variance). The

---

[8] This is the *mean amplitude*; tsunami waves at specific sites with large Q-factor and strong resonant properties may be much higher.

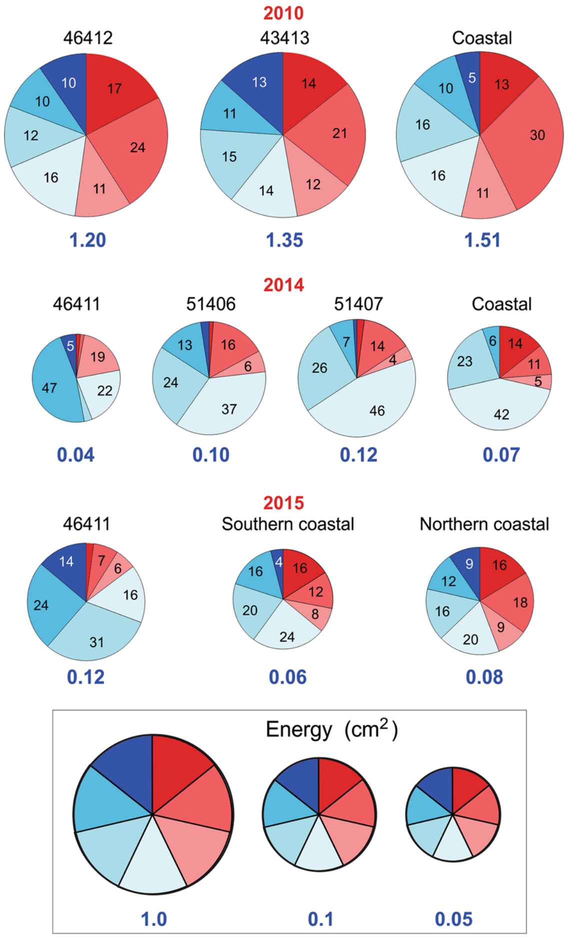

Figure 25
The integral tsunami energy, I_0, for the region offshore of Mexico for the 2010 (*upper panel*), 2014 (*middle panel*) and 2015 (*bottom panel*) events. The *area of a circle* is proportional to log(E); the total energy was estimated according to expression (11) based on the "true" tsunami spectra shown in Figs. 19b (2010), 21b (2014) and 23b (2015). The *different coloured* segments in a *circle* denote one of the seven frequency band partitions shown in spectra for these figures

results are shown in Fig. 25. The "reddish" circle (a circle with red colour prevalence) indicates dominance of low frequencies; "blueish" circles show dominance of high frequencies. The 2010 tsunami is clearly more "reddish" (more than 50 % of the total energy is on long periods, from 205 to 35 min), while the 2014 and 2015 tsunamis are more "blueish" (most of the energy is at periods <35 min). This difference is most certainly related to the length scale of the respective seismic source regions (Fig. 1). The source region was much larger for the 2010 event than for the two other events.

The "colour" of an event is important for the estimation of tsunami risk for a specific site. For sites with high-frequency resonant peaks (eigen periods), "blueish" tsunamis are especially dangerous; for sites located within long inlets or in large bays that have long fundamental periods, the major threat is from "reddish" tsunamis, as typified by long and narrow Alberni Inlet on the coast of British Columbia, which was strongly affected by the 1964 Great Alaska tsunami whose source that had a large extension and significant energy at low frequencies (cf. Rabinovich et al. 2013a).

The good agreement of the "colours" between open-ocean and coastal measurements is encouraging, in that it provides further support for our approach of using coastal measurements to reconstruct the characteristic features of open-ocean tsunamis.

The parameters introduced above describe generalized, open-ocean properties of tsunami waves. However, the results of our study also enable us to introduce a new form of "tsunami-zoning" (relative tsunami risk) for the Mexican coast based on tide gauge tsunami measurements of the three recent tsunamis originating off the coast of Chile. Maps showing maximum wave heights for each tsunami are presented in Figs. 5, 10 and 15. We can generalize these results. The individual maximum wave heights at each jth site, $H^j_{\max}$, can be used to evaluate the mean wave heights for the kth event,

$$\hat{H}^k_{\max} = \frac{1}{N_k}\sum_{j}^{N_k} H^{j_k}_{\max}. \qquad (13)$$

The corresponding $\hat{H}^k_{\max}$ values are: 98.7 cm (2010), 32.7 cm (2014) and 42.3 cm (2015). Findings reveal that the 2010 tsunami was roughly three times higher than the 2014 tsunami and 2.3 times higher than the 2015 tsunami.

To examine the response of individual sites to incoming tsunami waves, we introduce the *tsunami response coefficient*,[9]

---

[9] The physical sense of this coefficient is similar to the '*generation coefficient'* introduced by Šepić and Rabinovich (2014) to characterize the sea level response to small-scale atmospheric disturbances and the efficiency of meteotsunami generation along the East Coast of the United States.

$$A_j^k = \left(H_{\max}^{j_k}\right) / \left(\hat{H}_{\max}^k\right), \quad (14)$$

which enables us to specify sites with relatively strong ($A_j^k > 1.0$) or weak ($A_j^k < 1.0$) responses to arriving tsunami waves. The mean value of the tsunami response coefficient, $\hat{A}_j$, found by averaging A_j^k over all events, allows us to identify and map "hot" and "cold" tsunami impact sites along the Mexican coast (Fig. 26). The hottest spots, stations with maximum values of the tsunami response coefficient, are Puerto Angel ($\hat{A}_j = 1.77$), Puerto Madero (1.60) and Manzanillo (1.33). These are the sites having the maximum potential risk of large tsunami heights and associated extreme currents. In contrast, San Quintin ($\hat{A}_j = 0.17$), Mazatlan (0.43), La Paz (0.50) and Lazaro Cardenas (0.51) are sites with relatively low tsunami risk.

Figure 26, which is based on the analysis of three Chilean tsunamis, highlights the observation that the southern Pacific coast of Mexico is under much stronger tsunami risk than the northern coast. At the same time, we acknowledge that our estimates are of a preliminary nature and that for some sites were obtained on the basis of only one or two records. Moreover, the figure was generated using only "Chilean tsunamis" and would certainly benefit from similar maps based on transoceanic events originating from other regions of the Pacific Ocean. A prime example would be the 2011 Tohoku tsunami generated off the coast of Japan.

8. *Conclusions*

The three great Chilean earthquakes of 2010 (Maule, M_w 8.8), 2014 (Iquique, M_w 8.2) and 2015 (Illapel, M_w 8.3) generated major trans-Pacific tsunamis that were extensively recorded along the coast of Mexico. The 2010 tsunami was measured by seven tide gauges located at six sites, with maximum trough-to-crest wave heights observed at Acapulco (138 cm) and Manzanillo (134 cm). The 2014 tsunami was also detected at six sites, with maximum wave heights at Zihuatanejo (43 cm), Manzanillo (37 cm), Acapulco (36 cm) and Ensenada (36 cm). Twelve sites recorded the 2015 tsunami, with highest waves at Puerto Madero (85 cm), Puerto Angel (75 cm) and Manzanillo (64 cm). Based on analysis of the three tsunamis we identified and mapped "hot" and "cold" tsunami impact sites along the Mexican coast that are sites with higher and lower tsunami risk, respectively, associated with major trans-oceanic tsunamis.

This study combines coastal and open-ocean tsunami measurements. In all open-ocean DART records, and in certain coastal records with high signal-to-noise ratios, we find a "negative phase" arising from a small wave trough moving ahead of the main leading tsunami wave. These results support earlier findings of Rabinovich et al. (2013a), Watada et al. (2014) and Eblé et al. (2015) for the 2010, 2011, 2012 and 2014 tsunami events and, once again, demonstrate that a negative trough preceding a major arriving frontal crest wave is a consistent feature of strong trans-Pacific tsunamis. The main reason of this feature appears to be the Earth's crust subsidence under the gravitational loading of the propagating tsunami waves.

Another important outcome of our study is the use of spectral analysis methodology to reconstruct the "true" deep-ocean tsunami spectra based solely on an analysis of coastal tide gauge data. The "reconstructed" open-ocean tsunami spectra are in good agreement with the actual tsunami spectra evaluated from direct analysis of the DART records offshore of Mexico. We have further used the spectral estimates to parameterize the energy of the three Chilean tsunamis based on the total open-ocean tsunami energy and frequency content of the individual events.

The tsunami frequency bands for the three Chilean events were found to be significantly different. The band for the 2010 tsunami was from 0.2–0.25 to 30–40 cph, implying that the tsunami waves occupy a wide range of periods from 5–4 h to 2–1.5 min. The frequency band of the 2014 tsunami was narrower, from 0.7 to 20 cph (periods ~1.5 h to 3 min), with the maximum tsunami energy, $E_{\text{tsu}}(\omega)$, at 1–4 cph (60–15 min). For the 2015 tsunami, the tsunami frequency band was 0.4–30 cph (periods 2.5 h to 2 min), which was a little broader than for the 2014 tsunami but narrower than for the 2010 tsunami.

Spectral analysis enabled us to integrate the tsunami energy in the entire tsunami frequency band, $\omega_{\text{begin}} < \omega < \omega_{\text{end}}$, and estimate the 'integral tsunami energy' in the open ocean, I_0, a key parameter

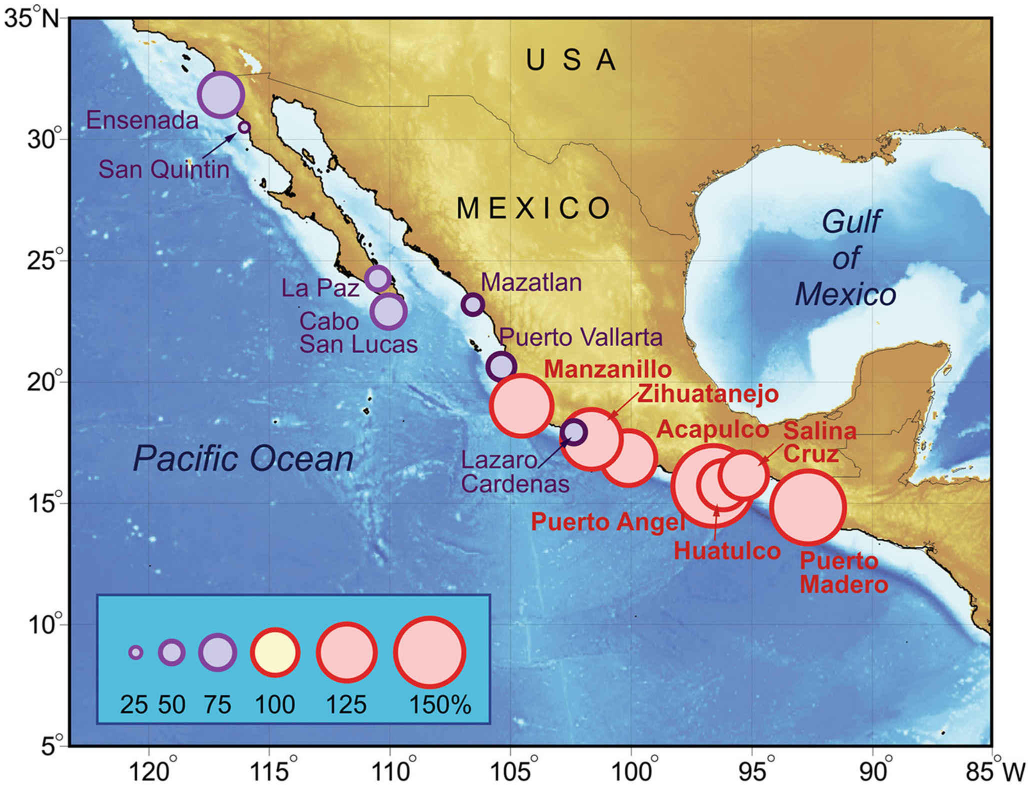

Figure 26
Map of coastal Mexico showing the '*tsunami response coefficients*' for various observational sites

characterizing the destructive potential of each event. We evaluated this parameter using both deep-ocean (DART) and coastal measurements and obtained very consistent results, with I_0 calculated from the coastal spectra in close agreement with I_0 calculated from open-ocean spectra. The mean value of I_0 for the three tsunamis was the following: 1.35 cm^2 (2010), 0.08 cm^2 (2014) and 0.09 cm^2 (2015). Comparison of this parameter with the mean tsunami variance at the coastal sites shows that tsunami waves propagating onshore from the open ocean amplify by approximately 20 times.

Another crucial characteristic of each tsunami event is the frequency content. Here, we chose to define the tsunami frequency content in terms of its "colour", in analogy with the classical light spectrum. Tsunamis range from red (low-frequency) to blue (high-frequency). "Red tsunamis" are of concern for long fjords, inlets, and other coastal basins with a long fundamental period of oscillations and prominent resonant properties. "Blue tsunamis" are of the highest concern for relatively small bays and harbours that have high Q-factors. In the case of the three Chilean tsunamis examined in this study, we separated the open-ocean tsunami spectra into seven partitions and estimated the relative tsunami variance for each of these partitions. Our results show that the 2010 tsunami was mainly "red" (low-frequency motions dominated), while the 2015 tsunami, and especially 2014 tsunami, were "blueish" (much more energy at high frequencies). It is clear that both the tsunami frequency bands and the "colour" of each event are determined by the characteristics of the source region, in particular the extension of the source area. These source attributes were the largest for the 2010 earthquake and the smallest for the 2014 earthquake.

We remark that, for all three Chilean tsunamis our estimates of tsunami "colour" (frequency composition) from the directly measured open-ocean tsunami spectra are also in close agreement with those obtained from the “reconstructed” coastal spectra. These results further support the analytical approaches developed in the present paper and demonstrate that it is possible to obtain reliable estimates of open-ocean tsunami parameters based solely on coastal tsunami wave measurements.

Acknowledgments

This work was partially supported by the Mexican National Polytechnic Institute (IPN, project SIP 20161036). Additional support for the first author was provided by SNI (Mexican National System of Investigators). For ABR this study was partly supported by the NOAA project WE-133R-15-SE-1608 and RSF Grant 14-50-00095. We gratefully acknowledge the Mexican National Mareographic Service of the UNAM and the Laboratory of the Sea Level of the CICESE for providing us the data of coastal sea level gauges, as well as George Mungov (NOAA/NCEI, Boulder, Colorado) for assisting us with the DART data. We also thank Vasily Titov and Rachel Tang (NOAA/PMEL, Seattle, WA) and Isaac Fine (IOS, Sidney, BC) for providing us the results of numerical modeling of the 2010, 2014 and 2015 Chilean tsunamis, Paul Whitmore and Stanley Goosby (NTWC, Palmer, AK) for presenting us precise ETAs for the three tsunamis recorded by DARTs 46412, 43412 and 43413 offshore of Mexico, and Maxim Krassovski (IOS, Sidney, BC) for helping with the figures.

References

An, C., Sepúlveda, I., & Liu, P. L.-F. (2014). Tsunami source and its validation of the 2014 Iquique, Chile, earthquake. *Geophysical Reseach Letters, 41*, 3988–3994. doi:10.1002/2014GL060567.

Aránguiz, R., González, G., González, J., Catalán, P. A., Cienfuegos, R., Yagi, Y., et al. (2016). The 16 September 2015 Chile tsunami from the post-tsunami survey and numerical modeling perspectives. *Pure and Applied Geophysics, 173*, 333–348. doi:10.1007/s00024-015-1225-4.

Borrero, J. C., & Greer, S. D. (2013). Comparison of the 2010 Chile and 2011 Japan tsunamis in the far field. *Pure and Applied Geophysics, 170*(6–8), 1249–1274. doi:10.1007/s00024-012-0559-4.

Calisto, I., Ortega, M., & Miller, M. (2015). Observed and modelled tsunami signals compared by using different rupture models of the April 1, 2014, Iquique earthquake. *Natural Hazards, 79*, 397–408. doi:10.1007/s11069-015-1848-x.

Calisto, I., Miller, M., & Constanzo, I. (2016). Comparison between tsunami signals generated by different source models and the observed data of the Illapel 2015 earthquake. *Pure and Applied Geophysics, 173*(4), 1051–1061. doi:10.1007/s00024-016-1253-8.

Candella, R. N., Rabinovich, A. B., & Thomson, R. E. (2008). The 2004 Sumatra tsunami as recorded on the Atlantic coast of South America. *Advances in Geosciences, 14*(1), 117–128.

Catalán, P. A., Aránguiz, R., González, G., et al. (2015). The 1 April 2014 Pisagua tsunami: Observations and modeling. *Geophysical Research Letters,*. doi:10.1002/2015GL063333.

Contreras-López, M., Winckler, P., Sepúlveda, I., Andaur-Álvarez, A., Cortés-Molina, F., Guerrero, C. J., et al. (2016). Field survey of the 2015 Chile tsunami with emphasis on coastal wetland and conservation areas. *Pure and Applied Geophysics, 173*(2), 349–367. doi:10.1007/s00024-015-1235-2.

Delouis, B., Nocquet, J.M., & Vallée M. (2010). Slip distribution of the February 27, 2010 $M_w = 8.8$ Maule earthquake, central Chile, from static and high-rate GPS, InSAR, and broadband teleseismic data. *Geophysical Research Letters, 37*, L17305. doi:10.1029/2009GL043899.

Eblé, M. C., Mungov, G., & Rabinovich, A. B. (2015). On the leading negative phase of major 2010–2014 tsunamis. *Pure and Applied Geophysics, 172*(12), 3493–3508. doi:10.1007/s00024-01.

Farreras, S. F., & Sanchez, A. J. (1991). The tsunami threat on the Mexican west coast: A historical analysis and recommendations for hazard mitigation. *Natural Hazards, 4*, 301–316.

Farreras, S. F., Ortiz, M., & González, J. I. (2007). Steps towards the implementation of a tsunami detection, warning, mitigation and preparedness program for south western coastal areas of Mexico. *Pure and Applied Geophysics, 164*, 605–616. doi:10.1007/s00024-006-0175-2.

Filloux, J. H., Luther, D. S., & Chave, A. D. (1991). Update on seafloor pressure and electric field observations from the north-central and northeastern Pacific: Tides, infratidal fluctuations, and barotropic flow. In B. B. Parker (Ed.), *Tidal hydrodynamics* (pp. 617–639). New York: J. Wiley.

Fine, I. V., & Thomson, R. E. (2013). A wavefront orientation method for precise numerical determination of tsunami travel time. *Natural Hazards and Earth Systems Sciences, 13*, 2863–2870. doi:10.5194/nhess-13-2863-2013.

Fine, I. V., Cherniawsky, J. Y., Thomson, R. E., Rabinovich, A. B., & Krassovski, M. V. (2015). Observations and numerical modeling of the 2012 Haida Gwaii tsunami off the coast of British Columbia. *Pure and Applied Geophysics, 172*(3–4), 699–718. doi:10.1007/s00024-014-1012-7.

Fritz, H. M., Petroff, C. M., Catalán, P. A., et al. (2011). Field survey of the 27 February 2010 Chile tsunami. *Pure and Applied Geophysics, 168*(11/12), 1989–2010. doi:10.1007/s00024-011-0283-5.

Fuentes, M., Riquelme, S., Hayes, G., Medina, M., Melgar, D., Vargas, G., et al. (2016). A study of the 2015 M_w 8.3 Illapel earthquake and tsunami: Numerical and analytical approaches. *Pure and Applied Geophysics, 173*, 1847–1858. doi:10.1007/s00024-016-1305-0.

Fujii, Y., & Satake, K. (2013). Slip distribution and seismic moment of the 2010 and 1960 Chilean earthquakes inferred from tsunami waveforms and coastal geodetic data. *Pure and Applied Geophysics, 170*(9–10), 1493–1509. doi:10.1007/s00024-012-0524-2.

Gusman, A. R., Murotani, S., Satake, K., Heidarzadeh, M., Gunawan, E., Watada, S., et al. (2015). Fault slip distribution of the 2014 Iquique, Chile, earthquake estimated from ocean-wide tsunami waveforms and GPS data. *Geophysical Research Letters, 42*(4), 1053–1060. doi:10.1002/2014GL062604.

Heidarzadeh, M., Satake, K., Murotani, S., Gusman, A. R., & Watada, S. (2015). Deep-water characteristics of the trans-Pacific tsunami from the 1 April 2014 M_w 8.2, Iquique, Chile earthquake. *Pure and Applied Geophysics, 172*(3–4), 719–730. doi:10.1007/s00024-014-0983-8.

Heidarzadeh, M., Murotani, S., Satake, K., Ishibe, T., & Gusman, A. R. (2016). Source model of the 16 September 2015 Illapel, Chile, M_w 8.4 earthquake based on teleseismic and tsunami data. *Geophysical Research Letters,*. doi:10.1002/2015GL067297.

Honda, K., Terada, T., Yoshida, Y., & Isitani, D. (1908). *An investigation on the secondary undulations of oceanic tides* (p. 108). J. College Sci., Imper. Univ. Tokyo.

Igarashi, Y. L., Kong, L., Yamamoto, M., & McCreery, C. S. (2011). Anatomy of historical tsunamis: Lessons learned for tsunami warning. *Pure and Applied Geophysics, 168*(11/12), 2043–2063. doi:10.1007/s00024-011-0287-1.

Kulikov, E. A., Rabinovich, A. B., Spirin, A. I., Poole, S. L., & Soloviev, S. L. (1983). Measurement of tsunamis in the open ocean. *Marine Geodesy, 6*(3–4), 311–329.

Kulikov, E. A., Rabinovich, A. B., & Thomson, R. E. (2005). Estimation of tsunami risk for the coasts of Peru and Northern Chile. *Natural Hazards, 35*(2), 185–209.

Lay, T., Yue, H., Brodsky, E. E., & An, C. (2014). The 1 April 2014 Iquique, Chile, M_w 8.1 earthquake rupture sequence. *Geophysical Research Letters, 41*, 3818–3825. doi:10.1002/2014GL060238.

Li, B., & Ghosh, A. (2016). Imaging rupture process of the 2015 Mw 8.3 Illapel earthquake using the US seismic array. *Pure and Applied Geophysics, 173*(7), 2245–2255. doi:10.1007/s00024-016-1323-y.

Miller, G. R. (1972). *Relative spectra of tsunamis* (p. 7). Hawaii Inst. Geophys, HIG-72-8.

Miller, G. R., Munk, W. H., & Snodgrass, F. E. (1962). Long-period waves over California's borderland. Part II, Tsunamis. *Journal of Marine Research, 20*(1), 31–41.

Mofjeld, H. O. (2009). Tsunami measurements. In A. Robinson & E. Bernard (Eds.), *The Sea*, vol. 15, Tsunamis (pp. 201–235). Cambridge, USA: Harvard University Press.

Mungov, G., Eblé, M., & Bouchard, R. (2013). DART® tsunameter retrospective and real-time data: A reflection on 10 years of processing in support of tsunami research and operations. *Pure and Applied Geophysics, 170*, 1369–1384. doi:10.1007/s00024-012-0477-5.

Omira, R., Baptista, M. A., & Lisboa, F. (2016). Tsunami characteristics along the Peru-Chile trench: analysis of the 2015 M_w 8.3 Illapel, the 2014 M_w 8.2 Iquique and the 2010 M_w 8.8 Maule tsunamis in the near-field. *Pure and Applied Geophysics, 173*(4), 1063–1077. doi:10.1007/s00024-016-1277-0.

Ortiz, M., Singh, S. K., Pacheco, J., & Kostoglodov, V. (1998). Rupture length of the October 9, 1995 Colima-Jalisco earthquake (M_w 8) estimated from tsunami data. *Geophysical Research Letters, 25*, 2857–2860.

Ortiz, M., Kostoglodov, V., Singh, S. K., & Pacheco, J. (2000). New constraints on the uplift of October 9, 1995 Jalisco-Colima earthquake (M_w 8) based on the analysis of tsunami records at Manzanillo and Navidad, Mexico. *Geofísica International, 39*, 349–357.

Pararas-Carayannis, G. (2010). The earthquake and tsunami of 27 February 2010 in Chile—evaluation of source mechanism and of near and far-field tsunami effects. *Science of Tsunami Hazards, 29*(2), 96–126.

Parker, B. B. (2007). Tidal analysis and prediction, NOAA Spec. Publ. NOS CO-OPS 3 (p. 378). Maryland: Silver Spring.

Rabinovich, A. B. (1997). Spectral analysis of tsunami waves: Separation of source and topography effects. *Journal Geophysical Research, 102*(C6), 12663–12676.

Rabinovich, A. B., & Eblé, M. C. (2015). Deep ocean measurements of tsunami waves. *Pure and Applied Geophysics, 172*(12), 3281–3312. doi:10.1007/s00024-015-1058-1.

Rabinovich, A. B., Thomson, R. E., & Stephenson, F. E. (2006). The Sumatra Tsunami of 26 December 2004 as observed in the North Pacific and North Atlantic Oceans. *Surveys in Geophysics, 27*, 647–677.

Rabinovich, A. B., Candella, R., & Thomson, R. E. (2011). Energy decay of the 2004 Sumatra tsunami in the World Ocean. *Pure and Applied Geophysics, 168*(11), 1919–1950. doi:10.1007/s00024-01-0279-1.

Rabinovich, A. B., Candella, R. N., & Thomson, R. E. (2013a). The open ocean energy decay of three recent trans-Pacific tsunamis. *Geophysical Research Letters,*. doi:10.1002/grl.50625.

Rabinovich, A. B., Thomson, R. E., & Fine, I. V. (2013b). The 2010 Chilean tsunami off the west coast of Canada and the northwest coast of the United States. *Pure and Applied Geophysics, 170*(9–10), 1529–1565. doi:10.1007/s00024-012-0541-1.

Sanchez, A. J., & Farreras, S. F. (1983). Maximum entropy spectral analysis of tsunamis along the Mexican coast, 1957–1979. In K. Iida & T. Iwasaki (Eds.), *Tsunamis: Their science and engineering* (pp. 147–159). Tokyo: Terra Sci.

Sanchez, A. J., & Farreras, S. F. (1993). *Catalog of Tsunamis on the Western Coast of Mexico* (p. 79). Boulder, CO: National Geophysical Data Center.

Šepić, J., & Rabinovich, A. B. (2014). Meteotsunami in the Great Lakes and on the Atlantic coast of the United States generated by the ''derecho'' of June 29–30, 2012. *Natural Hazards, 74*, 75–107. doi:10.1007/s11069-014-1310-5.

Shevchenko, G., Ivelskaya, T., Loskutov, A., & Shishkin, A. (2013). The 2009 Samoan and 2010 Chilean tsunamis recorded on the Pacific coast of Russia. *Pure and Applied Geophysics, 170*(9–10), 1511–1527. doi:10.1007/s00024-012-0562-9.

Stephenson, F. E., & Rabinovich, A. B. (2009). Tsunamis on the Pacific coast of Canada recorded in 1994–2007. *Pure and Applied Geophysics, 166*(1/2), 177–210. doi:10.1007/s00024-008-0440-7.

Tang, L., Titov, V. V., Bernard, E. N., Wei, Y., Chamberlin, C. D., et al. (2012). Direct energy estimation of the 2011 Japan tsunami using deep-ocean pressure measurements. *Journal of Geophysical Research, 117*, C08008. doi:10.1029/2011JC007635.

Tang, L., Titov, V. V., Moore, C., & Wei, Y. (2016). Real-time assessment of the 16 September 2015 Chile tsunami and implications for near-field forecast. *Pure and Applied Geophysics, 173*, 369–387. doi:10.1007/s00024-015-1226-3.

Thomson, R. E., & Emery, W. J. (2014). *Data analysis methods in physical oceanography* (3rd ed., p. 716). New York: Elsevier.

Thomson, R. E., Rabinovich, A. B., & Krassovski, M. V. (2007). Double jeopardy: Concurrent arrival of the 2004 Sumatra tsunami and storm-generated waves on the Atlantic coast of the United States and Canada. *Geophysical Research Letters, 34*, L15607. doi:10.1029/2007GL030685.

Thomson, R. E., Fine, I. V., Rabinovich, A. B., Mihaly, S. F., Davis, E. E., Heesemann, M., & Krassovski, M. V. (2011). Observations of the 2009 Samoa tsunami by the NEPTUNE-Canada cabled observatory: Test data for an operational regional tsunami model. *Geophysical Research Letters, 38*, L11701. doi:10.1029/2011GL046728.

Titov, V. V. (2009). Tsunami forecasting. In A. Robinson & E. Bernard (Eds.), *The Sea*, vol. 15, Tsunamis (pp. 371–400). Cambridge, USA: Harvard University Press.

Titov, V., Song, T., Tang, L., Bernard, E. N., Bar-Severt, Y., & Wei, Y. (2016). Consistent estimates of tsunami energy show promise for improved early warning. *Pure and Applied Geophysics,*. doi:10.1007/s00024-016-1312-1.

Tong, X., et al. (2010). The 2010 Maule, Chile earthquake: Down dip rupture limit revealed by space geodesy. *Geophysical Research Letters, 37*, L24311. doi:10.1029/2010GL045805.

Vich, M., & Monserrat, S. (2009). The source spectrum for the Algerian tsunami of 21 May 2003 estimated from coastal tide gauge data. *Geophysical Research Letters, 36*, L20610. doi:10.1029/2009GL039970.

Watada, S., Ksumoto, S., & Satake, K. (2014). Travel time delay and initial phase reversal of distant tsunamis coupled with the self-gravitating elastic Earth. *Journal of Geophysical Research: Solid Earth, 119*, 4287–4310. doi:10.1002/2013JB010841.

Wilson, R. I., Dengler, L. A., Legg, M. R., Long, K., & Miller, K. M. (2010). The 2010 Chilean tsunami on the California coastline. *Seismological Research Letters, 81*(3), 545–546.

Wilson, R. I., Admire, A. R., Borrero, J. C., Dengler, L. A., Legg, M. R., Lynett, P., et al. (2013). Observations and impacts from the 2010 Chilean and 2011 Japanese tsunamis in California (USA). *Pure and Applied Geophysics, 170*, 1127–1147. doi:10.1007/s00024-012-0527-z.

Ye, L., Lay, T., Kanamori, H., & Koper, K. D. (2016). Rapidly estimated seismic source parameter for the 16 September 2015 Illapel, Chile M_w 8.3 earthquake. *Pure and Applied Geophysics, 173*(2), 321–332. doi:10.1007/s00024-015-1202-y.

(Received August 20, 2016, revised September 21, 2016, accepted September 21, 2016, Published online October 27, 2016)